

A novel EFG meshless-ANN approach for static analysis of FGM plates based on the higher-order theory

Afsal K. P, K. Swaminathan, N. Indu & Sachin H

To cite this article: Afsal K. P, K. Swaminathan, N. Indu & Sachin H (2023): A novel EFG meshless-ANN approach for static analysis of FGM plates based on the higher-order theory, Mechanics of Advanced Materials and Structures, DOI: [10.1080/15376494.2023.2231459](https://doi.org/10.1080/15376494.2023.2231459)

To link to this article: <https://doi.org/10.1080/15376494.2023.2231459>



Published online: 13 Jul 2023.



Submit your article to this journal [↗](#)



Article views: 47



View related articles [↗](#)



View Crossmark data [↗](#)



Citing articles: 1 View citing articles [↗](#)

ORIGINAL ARTICLE



A novel EFG meshless-ANN approach for static analysis of FGM plates based on the higher-order theory

Afsal K. P, K. Swaminathan, N. Indu, and Sachin H

Departments of Civil Engineering, National Institute of Technology Karnataka, Mangaluru, India

ABSTRACT

An Element Free Galerkin (EFG) meshless formulation and solutions using higher order shear deformation theory with nine degrees of freedom for the static analysis of Functionally Graded Material (FGM) plates are provided. This technique estimates the shape function using Moving Least Squares (MLS) method. The proposed method is validated by comparing the present findings with those in the literature. A novel Artificial Neural Network (ANN) model is developed to forecast the deflection of FGM plates within less computational time. Detailed parametric and convergent studies reveal that the proposed EFG solution and the ANN technique are more efficient than their conventional counterparts. The validation and comparison of the generated results in the present investigation with the other analysis methods revealed that the EFG method and ANN model give more accurate results than the FEM and other meshless methods. The current EFG-ANN model reduces computing time by 99.94% when compared to the EFG approach. Also, the accuracy is enhanced using the EFG approach with HSDT9 for the FGM plate.

ARTICLE HISTORY

Received 25 April 2023
Accepted 24 June 2023

KEYWORDS

Static analysis; functionally graded plates; shear deformation; moving least square approximation; meshless method; artificial neural network

1. Introduction

Advanced technologies often require a peculiar combination of material properties that cannot be achieved with conventional materials like ceramics, polymers, and metal alloys. Hi-tech industries are constantly in search of innovative materials with exceptional blends of characteristics like lightweight, stiffness, strength, high temperature and corrosion resistance, toughness, and ductility. The most commonly used material that meets these requirements is Functionally Graded Material (FGM), which was first created by Japanese researchers in the late 1980s. FGMs are made up of two or many metals, and the volume fraction varies continuously and evenly over the intended dimensions of the FGM [1]. These materials prevent the occurrence of interface problems like debonding and cracks, which are often seen in composite laminated materials due to sudden changes in properties between adjacent layers. The exceptional characteristics of FGM make it a popular choice for use in structural elements in a variety of engineering fields, including aerospace, fusion reactors, automotive, marine, and defense technology.

Plate structures are the most commonly used in engineering's diverse fields. Typically, an FGM plate is made up of a metal and ceramic combination. Swaminathan et al. [2] conducted a panoramic study of many analytical and computational methods for the static, vibration, and buckling responses of FGM plates under mechanical and thermal loadings. Thai and Kim [3] classified the review according

to the Equivalent Single-Layer (ESL) models [4, 5], the three-dimensional elasticity theory, and the Carrera Unified Formulation (CUF) [6–10]. The mixed layer-wise models combine the advantages of both layer-wise and mixed theories, aiming to capture the complexities of the plate's mechanical response while maintaining computational efficiency. By incorporating multiple layers with different properties and considering the through-thickness variation, the mixed layer-wise models provide a more accurate representation of the mechanical behavior of multilayered plates [11–15]. By applying Reissner's mixed variational theorem, Carrera derived the equations of motion for the multilayered shell and incorporates various boundary conditions [16, 17]. Many theories have been developed for the static and free vibration analyses of FGM plates. The Classical Plate Theory (CPT) is the simplest ESL model [18, 19]. It is appropriate to be used for thin plates where the effects of transverse shear can be neglected. Reissner [20] and Mindlin [21] developed the First-order Shear Deformation Theory (FSDT) which takes into account the effect of transverse shear deformation using the shear correction factor. The shear correction factor cannot precisely predict the distribution of shear stress along the thickness direction. Hence Higher-order Shear Deformation Theories (HSDTs) [5, 22–25] were established to overcome the limitation posed by FSDT. Mohamed et al. [26] presented a comprehensive study on the bending behavior of FGM plates using a four-variable refined plate theory, which accounts for transverse shear deformation effects often neglected in classical plate theories.

Frahlia et al. [27] introduced a novel HSDT which provides a more accurate representation of the plate's behavior compared to traditional plate theories. Ma and Jin [28] developed a novel five-unknown plate theory for the analysis of plates.

Plates are analyzed using analytical as well as numerical methods. The solutions obtained from analytical methods are closer to the true value, but the process is tedious and time-consuming. Previously reported literature put forward a few analytic solutions that describe the mechanical behavior of FGM members using novel methods like the Symplectic framework approach [29–32]. Meanwhile, the numerical methods yield approximate results within a shorter span of time even for complex problems. Owing to the faster yet reliable results, Finite Element Method (FEM) [33–35] is used to analyze plates with complicated geometry [36] and a variety of boundary conditions. Despite the fact that it is a popular numerical technique for solving engineering problems, there are some drawbacks owing to the requirement of a predefined mesh and the difficulty in getting solutions in adaptive analysis, large deformation, and crack propagation problems, and mesh complexity problems in FGM plate with domain discontinuity [37, 38]. Hence, meshless methods have emerged as a viable option for solving Partial Differential Equations (PDE) in advanced computational engineering applications and have successfully attracted the attention of researchers in the last two decades [37, 39, 40].

Meshless methods are being utilized in diverse engineering applications, including the structural analysis of beams, plates, and shells. There are several variations of the meshless method, namely Smooth Particle Hydrodynamics (SPH) [41], Moving Least Square (MLS) method [42], Multi Quadric (MQ) method [43–45], Element Free Galerkin (EFG) method [46–48], Reproducing Kernel Particle (RKP) methods [49], Element Free Kp Ritz method [50, 51], Meshless Collocation (MC) method with Radial Basis Function (RBF) [52–56], Meshless Local Petrov-Galerkin (MLPG) method [57, 58], Point Interpolation (PI) method [59], Radial Point Interpolation (RPI) Method [59, 60], and Moving Kriging Interpolation (MKI) method [61, 62]. When it comes to formulating and solving plate problems with complicated geometries that are defined by partial differential equations and boundary conditions, the meshless technique has the unique advantage of not requiring the use of a mesh. Instead of a mesh, nodal points are utilized to break down the problem domain, and the shape function for every node is generated using the nodal points in the area it affects. This feature results in a more precise solution to problems with domain discontinuity in FGM plates, such as cutouts, crack growth, and corrosion.

Over the past two decades, numerous studies are published in the literature exploring the use of various meshless techniques, including the MLPG method [63–69], Collocation method [70–74], Kp-Ritz method [50, 75], MKI method [76–79], RKP method [80, 81], and RPI method [82], for analyzing the static and vibration behavior of FGM

plates. While meshless methods can solve complex geometry problems precisely, the corresponding computer code requires a long running time to obtain large results. If one can make use of this large database to create a prediction model which has the ability to learn and generalize from examples, the computational time can be reduced manifold. The technique of Artificial Neural Network (ANN) is a tool that can be used to forecast desired output from a set of inputs using a database of results.

An ANN imitates the flexible, simultaneous functioning of a healthy human brain. The ANN is now frequently used to solve complicated problems. Jodaei et al. [83] presented a three-dimensional investigation of functionally graded (FG) annular plates employing the state space-based differential quadrature method and comparative behavior modeling by ANNs for distinct boundary conditions. The validated results of the semi-analytical method were used to train and test the developed ANN model. Al Rjoub and Alshatnawi [84] studied the behavior of FGM plates with cracks and porosity. Using ANN technology, the natural frequency changes were predicted for porous FGM plates with a fractured side surface. The effects of cracking and porosity on the fundamental frequencies and mode shapes of FGM plates were studied. Employing the ANN technique, Vinayak et al. [85] built a predictive model to investigate how a sandwich plate made of skew laminated composite would respond to vibration in a humid, hot environment. Tran et al. [86] examined the behavior of FGM plates in a thermal environment resting on an elastic foundation. ANN was used to assess the vibrations of the FGM plates and forecast the results. ANN approach was adopted by Vinyas et al. [87] to predict the deflection of sandwich composite plates. Duong et al. [88] were primarily concerned about estimating the critical buckling load of FGM plates. The buckling loads of FGM plates under distinct boundary conditions and material combinations were evaluated using ANN modeling. Pham et al. [89] studied the free vibration response of auxetic honeycomb sandwich plates. In an attempt to improve the accuracy and computing efficiency of the analysis, an ANN was developed to assess and forecast the behavior of these plates. The major benefit of employing ANN models is that they contribute to faster computation and efficient resource use. Also, numerous data can be analyzed simultaneously by the ANN with minimal time expense.

Based on the above-discussed literature, it is perceived that the majority of research works done earlier are mostly confined to using the FSDT model and analytical solution methodology for the static analysis of FGM plates. But the analytical method is computationally strenuous to solve plate problems with different combinations of boundary conditions and complex geometry. To accurately predict the failure modes and to determine an optimal factor of safety in the design of machine parts and space structures, it is crucial to accurately determine displacements, stresses, strains, natural frequencies, and critical buckling load. An efficient displacement model and solution methodology are required to obtain such accurate results. Therefore, HSDTs that

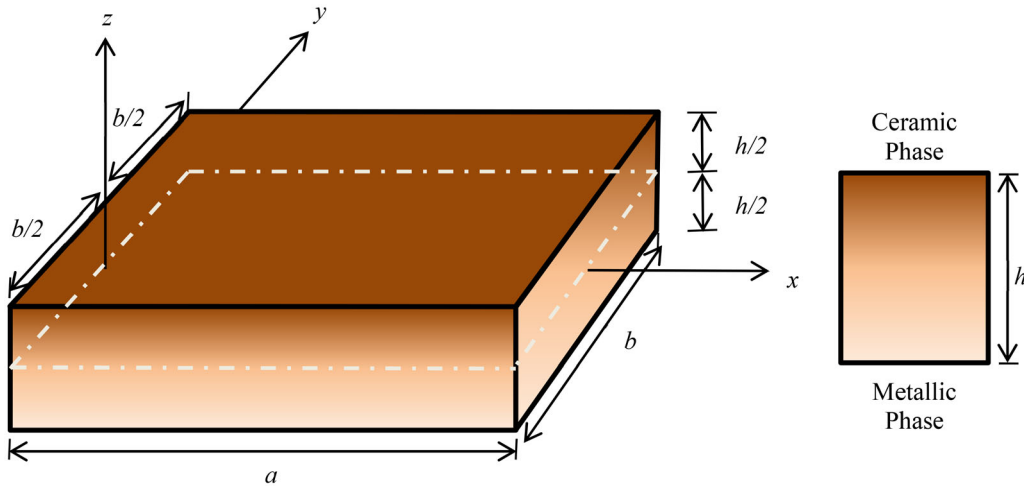


Figure 1. Schematic diagram of FGM plate and cross-section.

consider the realistic parabolic variation of the transverse shear along with a numerical solution technique such as the EFG method that offers greater accuracy with a faster convergence rate method are adopted. Such studies considering the EFG method with the higher-order displacement model remain unreported in the literature. Further, from the literature, it is found that ANN models are widely used for the prediction of responses of structural members, but the studies involving the ANN model with higher-order displacement models using the EFG method are not reported in the literature. Hence, In the present work ANN model with a higher-order displacement model (HSDT9) using the EFG method is developed. After developing the ANN model, the accuracy is established by comparing its results with previous findings from analytical, FEM, and other meshless methods. The field approximation in this study is made using the MLS approach with a cubic weight function. Initially, results from the EFG method are validated with results available in published literature. Thereafter more results are generated to develop an ANN model that predicts the transverse displacements at all points of the FGM plate. It is found that the current novel EFG-ANN model reduces the computation time effectively. In-house MATLAB code is developed to compute transverse displacements and generate an ANN model. Comprehensive parametric analyses are performed to examine the effects of boundary condition, volume fraction exponent, side-to-thickness ratio, aspect ratio, loading type, and material combination on the static behavior of FGM plates, and appropriate conclusions are presented.

2. Theoretical formulation

2.1. FGM plate

In this study, an FGM plate with dimensions $(a \times b \times h)$ and mid-plane located at $z=0$ is taken as the reference plane in the $(x-y-z)$ Cartesian coordinate system, illustrated in Figure 1. The material characteristics of the FGM plates are supposed to follow a power-law variation across the

plate thickness, as indicated by Eq. (1) presented below [90, 91].

$$E(z) = E_m + (E_c - E_m) \left(\frac{z}{h} + \frac{1}{2} \right)^p \quad (1)$$

$E(z)$ stands for Young's modulus, p represents the volume fraction exponent, and the subscripts "c" and "m" symbolize the ceramic and metallic components respectively.

2.2. Displacement model

The static analysis employs a polynomial-based HSDT with nine degrees of freedom that have previously been published in the literature [22]. This higher-order theory contemplates the realistic parabolic variation of the transverse shear deformation. The higher-order displacement field is expressed as:

$$\begin{aligned} u(x, y, z) &= u_0(x, y) + z\theta_x(x, y) + z^2 u_0^*(x, y) + z^3 \theta_x^*(x, y) \\ v(x, y, z) &= v_0(x, y) + z\theta_y(x, y) + z^2 v_0^*(x, y) + z^3 \theta_y^*(x, y) \\ w(x, y, z) &= w_0(x, y) \end{aligned} \quad (2)$$

The variables u , v , and w denote the displacements along the x , y , and z directions respectively. u_0 and v_0 refer to the in-plane displacements and w_0 refers to the transverse displacement of the point located at (x, y) on the central plane. θ_x and θ_y indicate rotations of the normal to the central plane around the y and x axes respectively. u_0^* , v_0^* , θ_x^* and θ_y^* are higher order terms that signify modes of transverse cross-sectional deformation and are described by Taylor series expansion.

The strain corresponding to the displacement model given by Eq. (2) can be expressed as,

$$\begin{aligned} \varepsilon_x &= \varepsilon_{x_0} + z\kappa_x + z^2 \varepsilon_{x_0}^* + z^3 \kappa_x^* \\ \varepsilon_y &= \varepsilon_{y_0} + z\kappa_y + z^2 \varepsilon_{y_0}^* + z^3 \kappa_y^* \\ \varepsilon_z &= 0 \\ \gamma_{xy} &= \varepsilon_{xy_0} + z\kappa_{xy} + z^2 \varepsilon_{xy_0}^* + z^3 \kappa_{xy}^* \\ \gamma_{yz} &= \phi_y + z\kappa_{yz} + z^2 \phi_y^* + z^3 \kappa_{yz}^* \\ \gamma_{xz} &= \phi_x + z\kappa_{xz} + z^2 \phi_x^* + z^3 \kappa_{xz}^* \end{aligned} \quad (3)$$

where

$$(\varepsilon_{x_0}, \varepsilon_{y_0}, \varepsilon_{z_0}, \varepsilon_{xy_0}) = \left(\frac{\partial u_0}{\partial x}, \frac{\partial v_0}{\partial y}, 0, \frac{\partial u_0}{\partial y} + \frac{\partial v_0}{\partial x} \right)$$

The bending stress resultant and strain relationship can be expressed as, $[\mathbf{N}^b]_{12 \times 1} = [\mathbf{C}^b]_{12 \times 12} [\boldsymbol{\varepsilon}^b]_{12 \times 1}$ where bending strain $\boldsymbol{\varepsilon}^b = \mathbf{B}^b \boldsymbol{\delta}$ and the shear stress resultant and strain relationship can be expressed as, $[\mathbf{N}^s]_{6 \times 1} = [\mathbf{C}^s]_{6 \times 6} [\boldsymbol{\varepsilon}^s]_{6 \times 1}$ where shear strain $\boldsymbol{\varepsilon}^s = \mathbf{B}^s \boldsymbol{\delta}$.

Where

$$\mathbf{N}^b = \{ N_x \quad N_y \quad N_{xy} \quad M_x \quad M_y \quad M_{xy} \quad N_x^* \quad N_y^* \quad N_{xy}^* \quad M_x^* \quad M_y^* \quad M_{xy}^* \}^T$$

$$\boldsymbol{\varepsilon}^b = \{ \varepsilon_{x_0}, \varepsilon_{y_0}, \varepsilon_{xy_0}, \kappa_x, \kappa_y, \kappa_{xy}, \varepsilon_{x_0}^*, \varepsilon_{y_0}^*, \varepsilon_{xy_0}^*, \kappa_x^*, \kappa_y^*, \kappa_{xy}^* \}^T$$

$$(\kappa_x, \kappa_y, \kappa_{xy}) = \left(\frac{\partial \theta_x}{\partial x}, \frac{\partial \theta_y}{\partial y}, \frac{\partial \theta_x}{\partial y} + \frac{\partial \theta_y}{\partial x} \right)$$

$$(\varepsilon_{x_0}^*, \varepsilon_{y_0}^*, \varepsilon_{xy_0}^*) = \left(\frac{\partial u_0^*}{\partial x}, \frac{\partial v_0^*}{\partial y}, \frac{\partial u_0^*}{\partial y} + \frac{\partial v_0^*}{\partial x} \right)$$

$$(\kappa_x^*, \kappa_y^*, \kappa_{xy}^*) = \left(\frac{\partial \theta_x^*}{\partial x}, \frac{\partial \theta_y^*}{\partial y}, \frac{\partial \theta_x^*}{\partial y} + \frac{\partial \theta_y^*}{\partial x} \right)$$

$$(\phi_x, \phi_y) = \left(\theta_x + \frac{\partial w_0}{\partial x}, \theta_y + \frac{\partial w_0}{\partial y} \right)$$

$$(\kappa_{xz}, \kappa_{yz}) = (2u_0^*, 2v_0^*)$$

$$(\phi_x^*, \phi_y^*) = (3\theta_x^*, 3\theta_y^*)$$

$$\mathbf{N}^s = \{ Q_x \quad Q_y \quad S_x \quad S_y \quad Q_x^* \quad Q_y^* \}^T$$

$$\boldsymbol{\varepsilon}^s = \{ \phi_x, \phi_y, \kappa_{xz}, \kappa_{yz}, \phi_x^*, \phi_y^* \}^T \quad (8a)$$

$$\boldsymbol{\delta} = \{ u_0 \quad v_0 \quad w_0 \quad \theta_x \quad \theta_y \quad u_0^* \quad v_0^* \quad \theta_x^* \quad \theta_y^* \}^T$$

$$[\mathbf{C}^b]_{12 \times 12} = \begin{bmatrix} \mathbf{A}_1 & \mathbf{A}_2 & \mathbf{A}_3 & \mathbf{A}_4 \\ \mathbf{A}_2 & \mathbf{A}_3 & \mathbf{A}_4 & \mathbf{A}_5 \\ \mathbf{A}_3 & \mathbf{A}_4 & \mathbf{A}_5 & \mathbf{A}_6 \\ \mathbf{A}_4 & \mathbf{A}_5 & \mathbf{A}_6 & \mathbf{A}_7 \end{bmatrix} \quad [\mathbf{C}^s]_{6 \times 6} = \begin{bmatrix} \mathbf{E}_1 & \mathbf{E}_2 & \mathbf{E}_3 \\ \mathbf{E}_2 & \mathbf{E}_3 & \mathbf{E}_4 \\ \mathbf{E}_3 & \mathbf{E}_4 & \mathbf{E}_5 \end{bmatrix}$$

$$(4) \quad \mathbf{A}_i = \begin{bmatrix} v_1 D_i & v_2 D_i & 0 \\ v_2 D_i & v_1 D_i & 0 \\ 0 & 0 & v_3 D_i \end{bmatrix}_{i=1 \text{ to } 7} \quad \mathbf{E}_i = \begin{bmatrix} v_3 D_i & 0 \\ 0 & v_3 D_i \end{bmatrix}_{i=1 \text{ to } 5} \quad (8b)$$

2.3. Constitutive relations

The Constitutive equations [92, 93, 94] are expressed as,

$$\begin{Bmatrix} \sigma_{xx} \\ \sigma_{yy} \\ \tau_{xy} \end{Bmatrix} = E(z) \begin{bmatrix} \frac{1}{(1-v^2)} & \frac{v}{(1-v^2)} & 0 \\ \frac{v}{(1-v^2)} & \frac{1}{(1-v^2)} & 0 \\ 0 & 0 & \frac{1}{2(1+v)} \end{bmatrix} \begin{Bmatrix} \varepsilon_{xx} \\ \varepsilon_{yy} \\ \gamma_{xy} \end{Bmatrix} \quad (5a)$$

$$\begin{Bmatrix} \tau_{yz} \\ \tau_{xz} \end{Bmatrix} = E(z) \begin{bmatrix} \frac{1}{2(1+v)} & 0 \\ 0 & \frac{1}{2(1+v)} \end{bmatrix} \begin{Bmatrix} \gamma_{yz} \\ \gamma_{xz} \end{Bmatrix} \quad (5b)$$

For an FGM plate, the stress resultant vector $\bar{\sigma}$ is expressed as,

$$\begin{bmatrix} N_x & M_x & N_x^* & M_x^* \\ N_y & M_y & N_y^* & M_y^* \\ N_{xy} & M_{xy} & N_{xy}^* & M_{xy}^* \end{bmatrix} = \int_{-h/2}^{h/2} \begin{Bmatrix} \sigma_x \\ \sigma_y \\ \sigma_z \\ \tau_{xy} \end{Bmatrix} [1 \quad z \quad z^2 \quad z^3] dz \quad (6)$$

$$\begin{bmatrix} Q_x & S_x & Q_x^* \\ Q_y & S_y & Q_y^* \end{bmatrix} = \int_{-h/2}^{h/2} \begin{Bmatrix} \tau_{xz} \\ \tau_{yz} \end{Bmatrix} [1 \quad z \quad z^2] dz \quad (7)$$

where

The \mathbf{B}^b and \mathbf{B}^s are strain displacement matrix,

$$[\mathbf{B}_i^b]_{12 \times 9} = \begin{bmatrix} \mathbf{b}_1^b & 0 & 0 & 0 & 0 \\ 0 & 0 & \mathbf{b}_1^b & 0 & 0 \\ 0 & 0 & 0 & \mathbf{b}_1^b & 0 \\ 0 & 0 & 0 & 0 & \mathbf{b}_1^b \end{bmatrix} \quad \text{Where,} \quad (9a)$$

$$\mathbf{b}_1^b = \begin{bmatrix} \frac{\partial \phi_i}{\partial x} & 0 \\ 0 & \frac{\partial \phi_i}{\partial y} \\ \frac{\partial \phi_i}{\partial y} & \frac{\partial \phi_i}{\partial x} \end{bmatrix}$$

$$[\mathbf{B}_i^s]_{6 \times 9} = \begin{bmatrix} \mathbf{0} & \mathbf{0} & \mathbf{b}_1^s & 0 & 0 \\ 0 & 0 & 0 & \mathbf{b}_2^s & 0 \\ 0 & 0 & 0 & 0 & \mathbf{b}_3^s \end{bmatrix} \quad (9b)$$

$$\begin{aligned} \mathbf{b}_1^s &= \begin{bmatrix} \frac{\partial \varphi_i}{\partial y} & 0 & \varphi_i \\ \frac{\partial \varphi_i}{\partial x} & \varphi_i & 0 \end{bmatrix} & \mathbf{b}_2^s &= \begin{bmatrix} 0 & 0 & 2\varphi_i \\ 0 & 2\varphi_i & 0 \end{bmatrix} \\ \mathbf{b}_3^s &= \begin{bmatrix} 0 & 0 & 3\varphi_i \\ 0 & 3\varphi_i & 0 \end{bmatrix} \end{aligned} \quad (9c)$$

2.4. MLS approximation

In the EFG approach, the MLS method is employed for the approximation of displacement. The general displacement field of a point of reference \mathbf{X} , say $u(x, y)$, is estimated in this technique by a displacement approximation function $u^h(\mathbf{X})$ of the form

$$\begin{aligned} u^h(\mathbf{X}) &= u^h(x, y) = \sum_{j=1}^m p_j(x, y) \alpha_j(x, y) = \mathbf{P}^T(x, y) \boldsymbol{\alpha}(x, y) \\ &= \mathbf{P}^T(\mathbf{X}) \boldsymbol{\alpha}(\mathbf{X}) \end{aligned} \quad (10)$$

The coefficients in the term $\boldsymbol{\alpha}(\mathbf{X}) = [\alpha_1(\mathbf{X}) \ \alpha_2(\mathbf{X}) \ \dots \ \alpha_m(\mathbf{X})]^T$ in Eq. (10) are functions of x, y that can be calculated by minimizing a function of weighted residuals. Where $\mathbf{P}^T(\mathbf{X})$ is the polynomial function. In this study, a two-dimensional linear basis polynomial is adopted.

$$\mathbf{P}^T(\mathbf{X}) = \mathbf{P}^T(x, y) = [1, x, y] \quad \text{where } m = 3 \quad (11)$$

$$J(\mathbf{X}) = \sum_{i=1}^n w(\mathbf{X} - \mathbf{X}_i) [\mathbf{p}^T(\mathbf{X}_i) \boldsymbol{\alpha}(\mathbf{X}) - u_i]^2 \quad (12)$$

Where m is the number of polynomial basis and n is the number of nodes in the neighborhood of \mathbf{X} , which is also named as the influence domain of \mathbf{X} . u_i is the unknown nodal parameter at a sampling node \mathbf{X}_i . $w(\mathbf{X} - \mathbf{X}_i)$ denotes a weight function. Minimizing $J(\mathbf{X})$ with respect to $\boldsymbol{\alpha}(\mathbf{X})$ produces the following linear system of equations.

$$\mathbf{A}(\mathbf{X}) \boldsymbol{\alpha}(\mathbf{X}) = \mathbf{B}(\mathbf{X}) \mathbf{u} \quad (13)$$

$$\boldsymbol{\alpha}(\mathbf{X}) = \mathbf{A}^{-1}(\mathbf{X}) \mathbf{B}(\mathbf{X}) \mathbf{u} \quad (14)$$

Where \mathbf{u} is $(n \times 1)$ vector consists of the nodal parameters of u_i in which the symmetric matrix $\mathbf{A}(\mathbf{X})$ is a weighted moment matrix $(m \times m)$ and the non-symmetric matrix $(m \times n)$ is $\mathbf{B}(\mathbf{X})$ and are defined as

$$\begin{aligned} \mathbf{A}(\mathbf{X}) &= \sum_{i=1}^n w_i(\mathbf{X}) \mathbf{p}(\mathbf{X}_i) \mathbf{p}^T(\mathbf{X}_i) \\ &= w_1(\mathbf{X}) \begin{bmatrix} 1 & x_1 & y_1 \\ x_1 & x_1^2 & x_1 y_1 \\ y_1 & x_1 y_1 & y_1^2 \end{bmatrix} + \dots \\ &+ w_n(\mathbf{X}) \begin{bmatrix} 1 & x_n & y_n \\ x_n & x_n^2 & x_n y_n \\ y_n & x_n y_n & y_n^2 \end{bmatrix} \end{aligned} \quad (15)$$

$$\begin{aligned} \mathbf{B}(\mathbf{X}) &= \begin{bmatrix} w_1(\mathbf{X}) \mathbf{p}(\mathbf{X}_1) & w_2(\mathbf{X}) \mathbf{p}(\mathbf{X}_2) & \dots & w_n(\mathbf{X}) \mathbf{p}(\mathbf{X}_n) \end{bmatrix} \\ &= \begin{bmatrix} w_1(\mathbf{X}) \begin{bmatrix} 1 \\ x_1 \\ y_1 \end{bmatrix} & w_2(\mathbf{X}) \begin{bmatrix} 1 \\ x_2 \\ y_2 \end{bmatrix} & \dots & w_n(\mathbf{X}) \begin{bmatrix} 1 \\ x_n \\ y_n \end{bmatrix} \end{bmatrix} \end{aligned} \quad (16)$$

Substituting Eq. (14) in Eq. (10) produces

$$\begin{aligned} u^h(\mathbf{X}) &= \sum_{j=1}^m p_j^T(\mathbf{X}) \left[\mathbf{A}^{-1}(\mathbf{X}) \mathbf{B}_i(\mathbf{X}) \right]_j u \\ &= \underbrace{\mathbf{p}^T(\mathbf{X}) \mathbf{A}^{-1}(\mathbf{X}) \mathbf{B}(\mathbf{X})}_{\boldsymbol{\varphi}^T(\mathbf{X})} \mathbf{u} = \boldsymbol{\varphi}^T(\mathbf{X}) \mathbf{u} = \sum_{i=0}^n \varphi_i(\mathbf{X}) u_i \end{aligned} \quad (17)$$

Where $\varphi_i(\mathbf{X}) = \mathbf{p}^T(\mathbf{X}) \mathbf{A}^{-1}(\mathbf{X}) \mathbf{B}_i(\mathbf{X})$ is the i th element of the MLS shape function.

$\boldsymbol{\varphi}^T(\mathbf{X}) = \mathbf{p}^T(\mathbf{X}) \mathbf{A}^{-1}(\mathbf{X}) \mathbf{B}(\mathbf{X}) = [\varphi_1(\mathbf{X}), \varphi_2(\mathbf{X}), \dots, \varphi_n(\mathbf{X})]$ is a vector of MLS shape functions. To calculate the derivatives from displacement, it requires the shape function's first derivative with respect to the spatial coordinates. Shape function is denoted as $\varphi_i(\mathbf{X}) = \gamma^T(\mathbf{X}) \mathbf{B}_i(\mathbf{X})$ where $\gamma(\mathbf{X}) = \mathbf{p}^T(\mathbf{X}) \mathbf{A}^{-1}(\mathbf{X})$ which leads to,

$$\mathbf{A}(\mathbf{X}) \gamma(\mathbf{X}) = \mathbf{p}(\mathbf{X}) \quad (18)$$

Derivative of Eq. (10) with respect to (x, y) and rearrange

$$\mathbf{A}(\mathbf{X}) \frac{\partial \gamma(\mathbf{X})}{\partial y} = \frac{\partial \mathbf{p}(\mathbf{X})}{\partial y} - \frac{\partial \mathbf{A}(\mathbf{X})}{\partial y} \gamma(\mathbf{X}) \quad (19)$$

$$\mathbf{A}(\mathbf{X}) \frac{\partial \gamma(\mathbf{X})}{\partial y} = \frac{\partial \mathbf{p}(\mathbf{X})}{\partial y} - \frac{\partial \mathbf{A}(\mathbf{X})}{\partial y} \gamma(\mathbf{X}) \quad (20)$$

An LU decomposition of the matrix $\mathbf{A}(\mathbf{X})$ which is then followed by back substitution, is used to derive the vector $\gamma(\mathbf{X})$, and its derivative $\gamma'(\mathbf{X})$.

Derivative of shape function with respect to x, y and rearrange

$$\frac{\partial \boldsymbol{\varphi}}{\partial x} = \frac{\partial \gamma^T(\mathbf{X})}{\partial x} \mathbf{B}_i(\mathbf{X}) + \gamma^T(\mathbf{X}) \frac{\partial \mathbf{B}_i(\mathbf{X})}{\partial x} \quad (21a)$$

$$\frac{\partial \boldsymbol{\varphi}}{\partial y} = \frac{\partial \gamma^T(\mathbf{X})}{\partial y} \mathbf{B}_i(\mathbf{X}) + \gamma^T(\mathbf{X}) \frac{\partial \mathbf{B}_i(\mathbf{X})}{\partial y} \quad (21b)$$

Because the MLS shape functions are referred to as approximants rather than interpolants and do not satisfy the Kronecker delta function property, the values attained through the MLS approximation differ from the nodal values, i.e. $u^h(x_i) \neq u_i$. These values are referred to as nodal parameters or fictional nodal values, as described in Figure 2.

The influence domain of \mathbf{X} might be any of square, rectangular, hexahedral, or circular shape. Rectangular domains are employed in this study. Weight functions are important in MLS approximation, and the cubic spline weight function is employed.

The weight function in one direction (cubic spline):

$$w(\mathbf{X}_x - \mathbf{X}_{ix}) = w(s) = \begin{cases} \frac{2}{3} - 4s_x^2 + 4s_x^3 & \text{for } s_x \leq \frac{1}{2} \\ \frac{4}{3} - 4s_x + 4s_x^2 - \frac{4}{3}s_x^3 & \text{for } \frac{1}{2} < s_x \leq 1 \\ 0 & \text{for } s_x > 1 \end{cases} \quad (22)$$

Where $s_x = \|x - x_i\| / (D_{mi})_x$ is the normalized radius, and $(D_{mi})_x$ is the x -direction domain of influence. In this study $(D_{mi})_x = 3.5$ are considered. Where $\|x - x_i\|$ is the absolute distance between the point of interest \mathbf{X}_x and the i^{th} node.

The first derivative of weight function in one direction:

$$\frac{dw_x}{dx} = \frac{dw_x}{ds_x} \frac{ds_x}{dx} = \begin{cases} (-8s_x + 12s_x^2) \times \text{sign}(x - x_i) & \text{for } s_x \leq \frac{1}{2} \\ (-4 + 8s_x - 4s_x^2) \times \text{sign}(x - x_i) & \text{for } \frac{1}{2} < s_x \leq 1 \\ 0 & \text{for } s_x > 1 \end{cases} \quad (23)$$

For the rectangular domain, a one-dimensional tensor product is utilized. The two-dimensional weight function of the i th node located at \mathbf{X} is calculated as follows:

$$w(\mathbf{X} - \mathbf{X}_i) = w(s_x) \times w(s_y) = w_x \times w_y \quad (24)$$

The derivative of the two-dimensional weight function is as follows:

$$\frac{dw}{dx} = \frac{dw_x}{dx} w_y \quad (25)$$

$$\frac{dw}{dy} = w_x \frac{dw_y}{dy} \quad (26)$$

2.5. EFG method

The Galerkin weak form of the equilibrium equation subject to essential and traction boundary conditions defined over the global domain is expressed as [37]

$$\int_{\Omega} \delta(\nabla u)^T \mathbf{C}(\nabla u) d\Omega - \int_{\Omega} \delta u^T b_f d\Omega - \int_{\Gamma_t} \delta u^T \bar{t} d\Gamma = 0 \quad (27)$$

Owing to the lack of the Kronecker delta function property in the MLS shape function utilized in the EFG meshless technique, several approaches have been devised to impose essential boundary conditions. The most widely used methods are the Lagrange multiplier method and the Penalty method. In this investigation, the Lagrange multiplier method is used to construct the constrained Galerkin weak form [37] which is written as

$$\int_{\Omega} \delta(\nabla u)^T \mathbf{C}(\nabla u) d\Omega - \int_{\Omega} \delta u^T b_f d\Omega - \int_{\Gamma_t} \delta u^T \bar{t} d\Gamma - \int_{\Gamma_u} \delta \lambda^T (u - \bar{u}) d\Gamma - \int_{\Gamma_u} \delta u^T \lambda d\Gamma = 0 \quad (28)$$

Where the vector of Lagrange multipliers represented by λ , is utilized to implement the essential boundary conditions, i.e. $u - \bar{u} = 0$.

The final static discrete system of equation is presented as

$$\begin{bmatrix} \mathbf{K} & \mathbf{G} \\ \mathbf{G}^T & \mathbf{0} \end{bmatrix} \begin{Bmatrix} \mathbf{u} \\ \lambda \end{Bmatrix} = \begin{Bmatrix} \mathbf{F} \\ \mathbf{q} \end{Bmatrix} \quad (29)$$

Where the global stiffness matrix represented by \mathbf{K} has its elements obtained by solving Eq. (30a). The remaining parameters are derived from solving Eq. (30b).

$$K_{ij} = \int_{\Omega} \mathbf{B}_i^T \mathbf{D} \mathbf{B}_j d\Omega \quad (30a)$$

$$G_{ik} = - \int_{r_u} \varphi_i \mathbf{N}_k d\Gamma$$

$$f_i = \int_{r_t} \varphi_i \bar{t} d\Gamma + \int_{\Omega} \varphi_i b_f d\Omega \quad \text{Where, } \mathbf{N}_k = \begin{bmatrix} N_k & 0 & \ddots \\ 0 & \ddots & 0 \\ \ddots & 0 & N_k \end{bmatrix}_{(DOF \times nc)}$$

$$q_k = - \int_{r_u} N_k \bar{u} d\Gamma$$

$$(30b)$$

DOF and nc are the degree of freedom and the number of constraints at each node. In Eqns. (30), the conventional Gauss quadrature method is used for numerical integration in the background cells.

2.6. Artificial neural network

The ANN is a computer model comprised of numerous interconnected processing units called neurons. These basic units called neurons work together in parallel to perform mathematical operations on inputs and produce outputs. This system is inspired by the human brain and is often utilized in pattern recognition and data fitting. Once trained, an ANN can make predictions or estimations using new, independent data. It is made up of three main components known as the input layer, the hidden layers, and the output layer, which are connected by synapses to allow for the flow of information. The aim of the connections among the neurons and the bias value of the neurons is to bring the difference between the output of ANN and the actual output of the problem to the least possible value. Each neuron receives inputs x_i , connected to the weights (w_i) which show the strength of the connection for that input. The weights of the neuron connections are then multiplied by each input. Additionally, a bias (b_i) is introduced as a connection weight

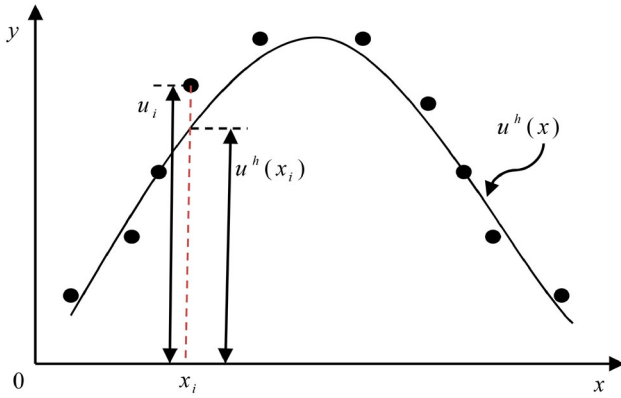


Figure 2. Approximations diagram of Moving least squares.

that has a constant value added to the sum of inputs and their corresponding weights as expressed as

$$z_i = \sum_{j=1}^H w_{ij}x_j + b_i \quad (31)$$

The result of the sum z_i is transformed by a function known as the transfer or activation function $f(z_i)$, producing an output value referred to as the “activation” of the unit, expressed by

$$Y_i = f(z_i) \quad (32)$$

The activation functions enable artificial neural networks to exhibit the non-linearity that grants them their formidable power. Until reaching the output layer, the neuron sends a signal to the next layer’s nodes through a transfer function. Each hidden layer is equipped with a bias node to either advance or retract the activation function. There are various types of activation functions, such as Linear, Saturating Linear, Log-Sigmoid, ReLu, Tan-Sigmoid, Symmetrical Hard Limit, etc. Popular ANN training algorithms include Levenberg–Marquardt, Bayesian Regularization, Quasi-Newton, etc. In this study, the “hyperbolic tangential sigmoid” function (tansig) is selected as the activation function, and the “Levenberg–Marquardt” algorithm (trainlm) incorporated into a MATLAB program will be utilized to train the network. The weights linked to each connection vary along with the learning process until the desired outputs are achieved.

At the start of network initialization, random values are assigned to these weights, and they undergo ongoing modifications throughout the training process. The process of training is repeated with adjusted weights until the desired results are achieved. The ANN model is to consider eight boundary conditions, E_c/E_m ratio, uniform, and bi-sinusoidal load types, aspect ratio (b/a), side-to-thickness ratio (a/h), power law index (p), and plate coordinates x and y to obtain the dimensionless transverse displacement as the output. But when the eight boundary conditions are given as inputs, the accuracy of the model is badly affected. So, eight distinct models corresponding to eight different boundary conditions are developed and combined into a single ANN model for greater accuracy. The ANN network architecture comprises eight inputs and one output. The input layer has eight neurons, each receiving direct input data (direct connection)

Table 1. Materials that were used to make the FGM plate.

Properties	E (GPa)	ρ (kg/m ³)	ν
Aluminum (Al)	70	2702	0.3
Zirconia (ZrO ₂)	200	5700	0.3
Alumina (Al ₂ O ₃)	380	3800	0.3

Table 2. Convergence of dimensionless transverse displacements \bar{w} of an Al/Al₂O₃ square plate under UDL and BSL ($a/h = 10$).

Nodes division	\bar{w}				
	$p = 0$	$p = 1$	$p = 3$	$p = 5$	$p = 10$
Uniform load					
4 × 4	0.4580 (98.20%)	0.9316 (99.67%)	1.3248 (99.64%)	1.4405 (99.62%)	1.5928 (99.60%)
8 × 8	0.4659 (98.89%)	0.9274 (99.88%)	1.3187 (99.89%)	1.4336 (99.90%)	1.5849 (99.91%)
10 × 10	0.4659 (98.89%)	0.9275 (99.89%)	1.3189 (99.91%)	1.4337 (99.91%)	1.5850 (99.91%)
16 × 16	0.4662 (99.96%)	0.9282 (99.97%)	1.3198 (99.98%)	1.4346 (99.97%)	1.5860 (99.97%)
22 × 22	0.4664 (100%)	0.9285 (100%)	1.3201 (100%)	1.4350 (100%)	1.5864 (100%)
26 × 26	0.4664 (100%)	0.9285 (100%)	1.3201 (100%)	1.4350 (100%)	1.5864 (100%)
Analytical HSST-9 [95]	0.4666	0.9266	1.3187	1.4338	1.5847
Bi-sinusoidal load					
4 × 4	0.2910 (98.28%)	0.5865 (99.58%)	0.8349 (99.59%)	0.9086 (99.62%)	1.0054 (99.64%)
6 × 6	0.2964 (99.90%)	0.5895 (99.92%)	0.8391 (99.90%)	0.9131 (99.89%)	1.0102 (99.88%)
8 × 8	0.2961 (100%)	0.5890 (100%)	0.8383 (100%)	0.9122 (99.99%)	1.0091 (99.99%)
10 × 10	0.2961 (100%)	0.5890 (100%)	0.8383 (100%)	0.9121 (100%)	1.0090 (100%)
14 × 14	0.2961 (100%)	0.5890 (100%)	0.8383 (100%)	0.9121 (100%)	1.0090 (100%)
Analytical GSDT [96]	0.2960	0.5889	0.8377	0.9118	1.0089

Values given within the bracket are the percentage of convergence.

where data transfer is done using the hyperbolic tangential sigmoid function (tansig) function, as shown in Figure 3. The ideal number of neurons and the suitable activation function were determined via trial and error. The data transfer from the input layer to the first hidden layer and between the hidden layers (each containing twenty neurons with dense connection) uses the tansig function. In contrast, the transfer of data from the last hidden layer to the output layer is carried out using a linear activation function (purelin).

3. Results and discussions

In this section, some numerical examples are provided to showcase the accuracy of the EFG method in predicting the static responses of FGM plates using the HSST9 model. Table 1 lists the properties of three different types of materials used in the analysis. Figure 4 depicts the eight various boundary conditions that are considered. Support conditions are denoted by the letters “S,” “C,” and “F,” which stand for simply supported, clamped, and free end conditions. The plate stiffness and mass matrices are evaluated using a 3 × 3 Gauss quadrature integration for static analysis. The results based on different solution methods are compared with the EFG meshless solutions obtained in the present investigation using the HSST9 model. For an arbitrary edge with simply supported and clamped edge conditions, the boundary conditions are as follows:

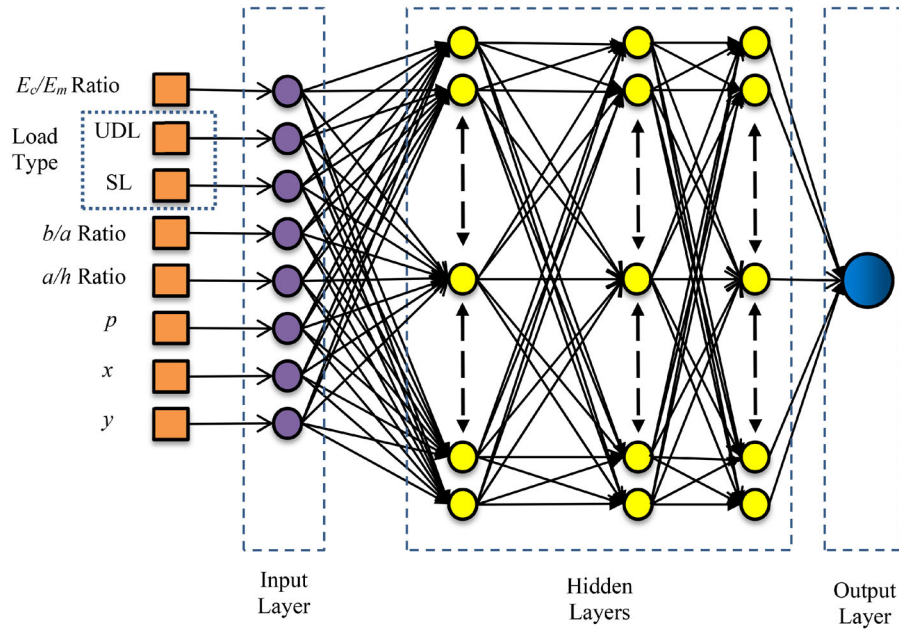


Figure 3. The architecture of the developed ANN predictive model.

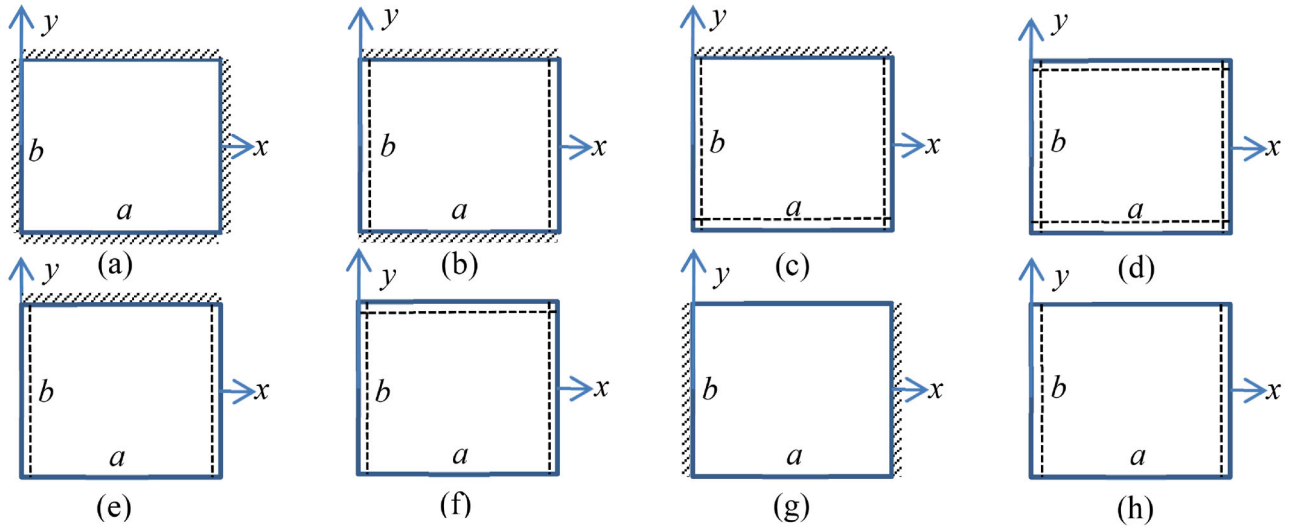


Figure 4. Different boundary conditions of FGM plate (a) CCCC, (b) SCSC, (c) SSSC, (d) SSSS, (e) SFSC, (f) SFSS, (g) CFCF and (h) SFSF.

Simply supported (S): $v_0, w_0, \theta_y, v_0^*, \theta_y^* = 0$ at $x = 0, a$

$: u_0, w_0, \theta_x, u_0^*, \theta_x^* = 0$ at $y = -b/2, +b/2$

Clamped (C) : $u_0, v_0, w_0, \theta_x, \theta_y, u_0^*, v_0^*, \theta_x^*, \theta_y^* = 0$ at $x = 0, a$ and $y = -b/2, +b/2$

The following non-dimensional forms are used:

$$\bar{w} = w \left(\frac{10h^3 E_c}{P_0 a^4} \right), \quad \hat{w} = w \left(\frac{100h^3 E_m}{12(1 - \nu^2) P_0 a^4} \right) \quad (33)$$

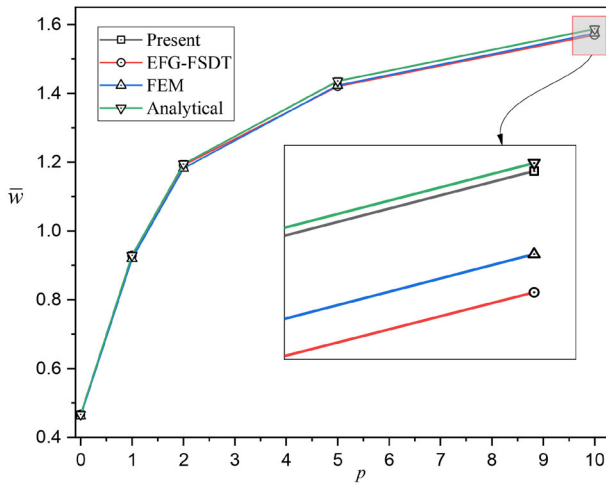
3.1. Convergence studies

The study aims to determine the number of nodes needed for the transverse displacements of an SSSS square plate with Al/Al₂O₃ material properties under Uniform Distributed Load (UDL) and Bi-Sinusoidal Load (BSL) to

converge. The plate's side-to-thickness ratio is set to 10, and different values of volume fraction exponent p are considered. The convergence of dimensionless transverse displacement is given in Table 2 and the results are compared with the analytical solutions from Tu Minh et al. [95] based on HSDT9 and Zenkour [96] based on Generalized Shear Deformation Theory (GSDT). The study shows that increasing the number of nodes leads to solutions that approach the analytical solutions, and the convergence of EFG meshless solutions and analytical solutions is almost exact. The study concludes that a node division of 22×22 (529 Nodes) is needed for the dimensionless transverse displacements under uniform load to converge, while a node division of 10×10 (121 Nodes) is required for the bi-sinusoidal load. These convergent node divisions are used for comparison, validation, and parametric studies.

Table 3. Comparison of dimensionless transverse displacements \bar{w} of an Al/Al₂O₃ square plate under uniform load.

a/h	Method	\bar{w}				
		$p=0$	$p=1$	$p=2$	$p=5$	$p=10$
2	Present	1.0116	1.8507	2.4708	3.4855	4.1063
	EFG-FSDT	1.0181	1.8603	2.4001	3.1431	3.7044
	FEM	1.0117	1.8506	2.4707	3.4855	4.1065
	Analytical [95]	1.0116	1.8511	2.4708	3.4822	4.1009
5	Present	0.5350	1.0446	1.3555	1.6951	1.9051
	EFG-FSDT	0.5355	1.0451	1.3419	1.6356	1.8363
	FEM	0.5339	1.0421	1.3524	1.6919	1.9019
	Analytical [95]	0.5354	1.0454	1.3568	1.6970	1.9071
10	Present	0.4664	0.9285	1.1941	1.4350	1.5864
	EFG-FSDT	0.4665	0.9286	1.1907	1.4202	1.5694
	FEM	0.4624	0.9191	1.1822	1.4231	1.5748
	Analytical [95]	0.4666	0.9289	1.1947	1.4360	1.5875
20	Present	0.4491	0.8993	1.1535	1.3698	1.5066
	EFG-FSDT	0.4492	0.8994	1.1527	1.3662	1.5025
	FEM	0.4339	0.8633	1.1079	1.3245	1.4624
	Analytical [95]	0.4494	0.8997	1.1541	1.3705	1.5074

**Figure 5.** Comparison of dimensionless transverse displacement \bar{w} with analytical and FEM methods under SSSS boundary condition of an Al/Al₂O₃ square plate ($a/h = 10$).

3.2. Comparison and validation studies

Comparison and validation studies of the EFG method for static analysis of FGM plates are presented in the first section. In the subsequent section, the accuracy of the developed ANN model is evaluated by comparing it with analytical and EFG solutions.

3.2.1. EFG method

Example 1. The study examines an Al/Al₂O₃ FGM plate, which is supported at all edges and subject to UDL. Table 3 provides a comparison of dimensionless transverse displacements for different volume fraction exponent (p) and side-to-thickness ratio (a/h). The EFG meshless method is used to obtain the solutions, which are compared with analytical and conventional FEM solutions using four-noded elements. Both methods use the HSDT9 displacement model. The study aims to present the accuracy of the presented method in the prediction of displacement, compare its accuracy with conventional FEM, and examine the effect of considering shear deformation in the EFG method.

Table 4. Comparison of dimensionless transverse displacements \hat{w} of an Al/ZrO₂ square plate under UDL ($a/h = 5$).

BC's	Theory	\hat{w}			
		$p=0$	$p=0.5$	$p=1$	$p=2$
SSSS	Present	0.1715	0.2318	0.2717	0.3135
	MLPG [64]	0.1671	0.2505	0.2905	0.3280
	Kp-Ritz [50]	0.1722	0.2403	0.2811	0.3221
	Analytical	0.1716	0.2319	0.2719	0.3138
CCCC	Present	0.0762	0.1011	0.1186	0.1395
	MLPG [64]	0.0731	0.1073	0.1253	0.1444
	Kp-Ritz [50]	0.0735	0.1034	0.1207	0.1404
SCSC	Present	0.1070	0.1427	0.1675	0.1961
	Meshless-MLPG [64]	0.1017	0.1501	0.1751	0.2008
	Kp-Ritz [50]	0.1073	0.1447	0.1701	0.2008

The FEM method requires a larger node division of 44×44 (2025 Nodes) compared to the EFG method (529 Nodes) for convergence. Results obtained from the EFG method show excellent agreement with the analytical method and perform better than FEM (see Table 3 and Figure 5). Table 3 also compares the results obtained using the EFG method with FSDT and HSDT9 examples, which suggests that considering the transverse shear deformation effect is essential for the static analysis of the FGM plate when the volume fraction exponent p increases.

Example 2. This example is to illustrate the accuracy of the EFG meshless method in the prediction of static displacement of an Al/ZrO₂ FGM square plate with various boundary conditions under UDL, in comparison to other meshless methods. The study compares the dimensionless transverse displacements (\hat{w}) in Table 4 for distinct values of the volume fraction exponent (p), with an FGM plate having a value of $a/h = 5$. The EFG meshless results are compared with analytical solutions based on the HSDT9 displacement model and other meshless methods, namely the MLPG method [64] based on the HOSNDPT (Higher Order Shear and Normal Deformable Plate Theory) displacement model and the KP-Ritz method [50] based on the FSDT displacement model. The study shows that the EFG meshless method outperforms the MLPG and KP-Ritz meshless methods in terms of accuracy (Figure 6).

Example 3. This example is presented to establish the accuracy of the EFG meshless method in the evaluating static displacement of an Al/Al₂O₃ square FGM plate. Here FGM plates with various boundary conditions and subjected to bi-sinusoidal load are considered. The transverse displacements obtained from the current EFG meshless formulation are compared with the displacement found in published literature works from Mantari et.al. [9], Carrera. et.al. [97] and Thai et al. [98]. It should be noted that Mantari et.al et al. [9] incorporated CUF, while Carrera. et.al. [97] considered Quasi-3D and Thai et al. [98] made use of Four Variable Theory (FVT) to obtain transverse displacements. The comparison study is tabulated in Table 5 for distinct values of the volume fraction exponent (p) and varying a/h , of an FGM plate. It is found that the present results are good agreement with results already published by other authors.

3.2.2 ANN model

An ANN is applied to the current problem, with a separate model being developed for each of the eight boundary conditions. These different models are combined together to yield accurate results. Around 16,77,906 points to each

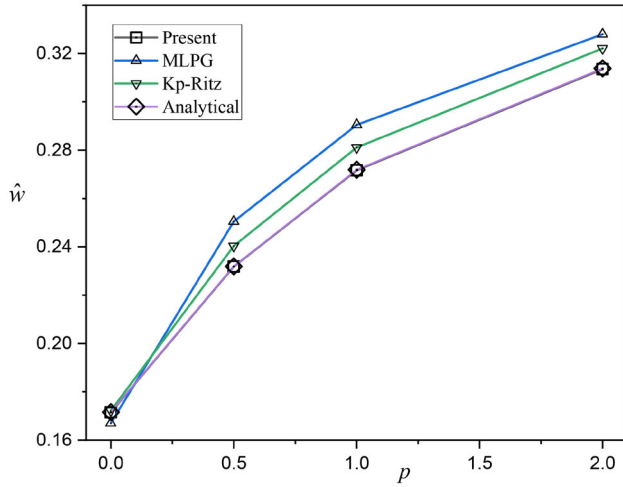


Figure 6. Comparison of dimensionless transverse displacement \hat{w} with other meshless methods under UDL and SSSS boundary condition of an Al/ZrO₂ square plate ($a/h = 5$).

Table 5. Comparison of dimensionless transverse displacements \hat{w} of an Al/Al₂O₃ square plate under BSL.

a/h	Method	$p = 1$	$p = 4$	$p = 10$
4	Mantari et.al. [9]	0.7171	1.1585	1.3745
	Carrera. et.al. [97]	0.7171	1.1585	1.3745
	Thai. et.al. [98]	0.7308	1.1625	1.3952
	Present	0.7289	1.1646	1.3919
10	Mantari et.al. [9]	0.5875	0.8821	1.0072
	Carrera. et.al. [97]	0.5875	0.8821	1.0072
	Thai. et.al. [98]	0.5914	0.8840	1.0131
	Present	0.5890	0.8823	1.0089
100	Mantari et.al. [9]	0.5625	0.8286	0.9361
	Carrera. et.al. [97]	0.5625	0.8286	0.9361
	Thai. et.al. [98]	0.5649	0.8312	0.9406
	Present	0.5581	0.8231	0.9309

model are collected from an EFG meshless solution with a wide range of variables considered, including material combinations, loading conditions, and geometric properties. The developed ANN architecture is trained using non-dimensional transverse displacement \bar{w} values as mentioned in Eq. (33) obtained from the EFG method. The input data include aspect ratio (b/a), thickness ratio (a/h), power law index (p), boundary conditions, E_c/E_m ratio, load type and the output is the displacement (\bar{w}). The variables relating to material viz., the ratio (E_c/E_m) and volume fraction exponent (p) values are within a range of [1:7] and [0:10], respectively. The geometric variables, aspect ratio (b/a) and thickness ratio (a/h), range between [2:100] and [1:5] respectively.

The performance of an ANN is evaluated by the Mean Square Error (MSE) and Pearson's correlation coefficient (R). For perfect fitting data, the correlation coefficient becomes unity, where the outputs from the neural network precisely match the values in the testing subset, the y-intercept is 0 and the slope of the line is 1. Here, eight ANN models are developed for eight different boundary conditions. The training and testing of the ANN model for all edges simply-supported (SSSS) case show R values as 0.99999 and 0.99995 respectively. Each model is trained for uniformly and sinusoidally loaded plates with E_c/E_m ratio ranging from 1 to 7 (1,2,3,4,5,7), aspect ratio ranging from 0.5 to 5 (0.5,1,1.5,2,3,4,5), thickness ratio 2 to 100 (2,4,10,20,50,100), and p value ranging from 0 to 10 (0,0.5,1,2,5,8,10). The regression, performance, error histogram, and training state plots of the SSSS case are shown in Figures 7 and 8 respectively. Each model is tested for uniformly loaded plates with E_c/E_m ratios 1.25 and 3, aspect ratios 2.5 and 4.5, thickness ratios 5 and 25, and p values ranging from 0 to 10 (0,0.75,1,2,10). The testing R-value and error histogram plots are provided in Figure 9. The R-value and mean squared error (performance) values of all ANN models for training and testing corresponding to eight boundary conditions are given in Table 6.

The comparison study of the results of the ANN model with analytical and EFG solutions in terms of accuracy is

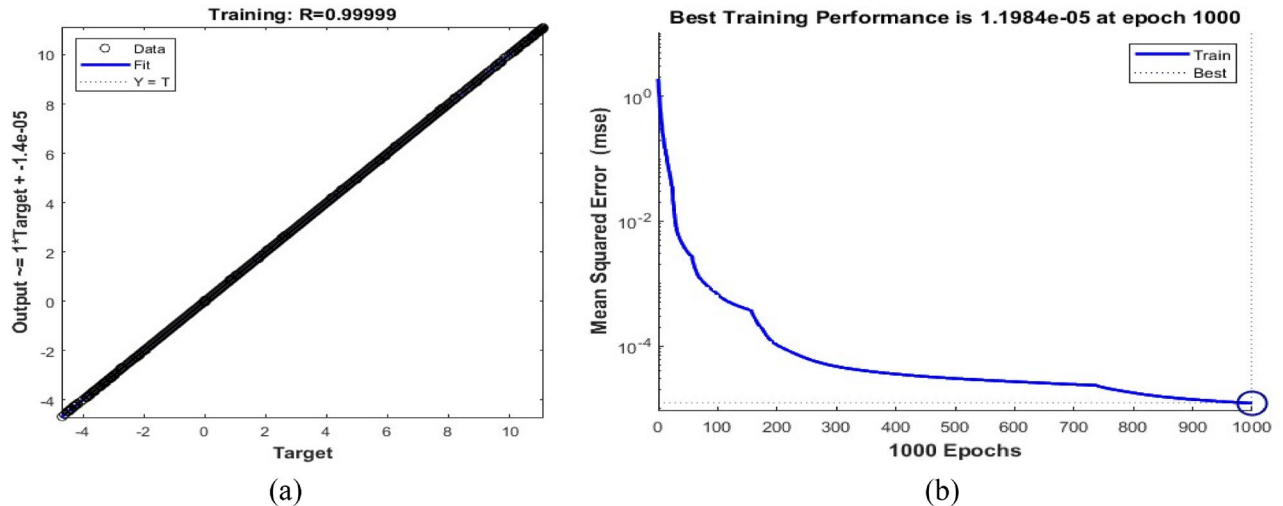


Figure 7. Regression and performance results of training of neural network for SSSS rectangular FGM plate. (a) Regression plot and (b) Performance plot.

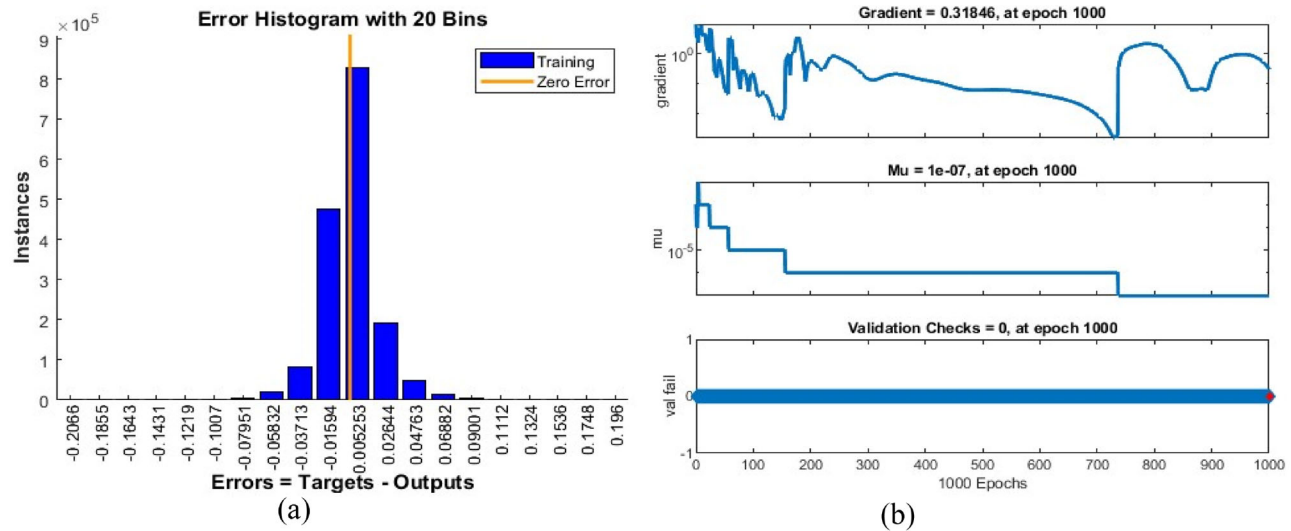


Figure 8. Schematic representation of developed ANN predictive model for SSSS FGM plate (a) Error histogram of training and (b) Training state.

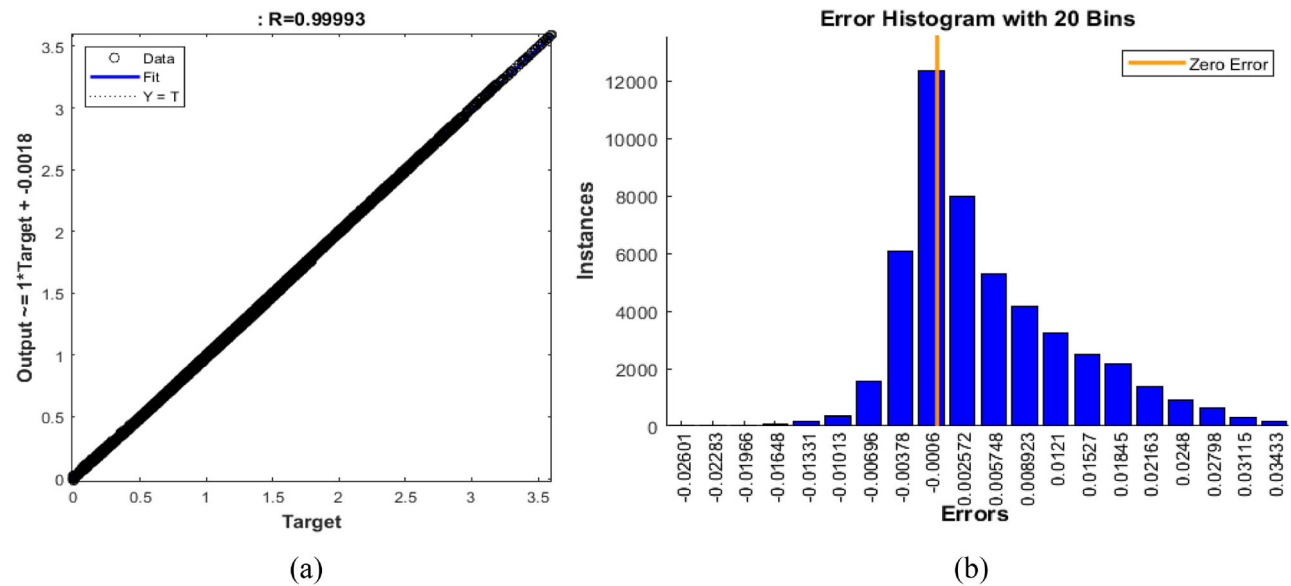


Figure 9. Results of testing of neural network for SSSS FGM plate (a) Regression plot and (b) Error histogram.

Table 6. EFG-ANN model performance results for all boundary conditions.

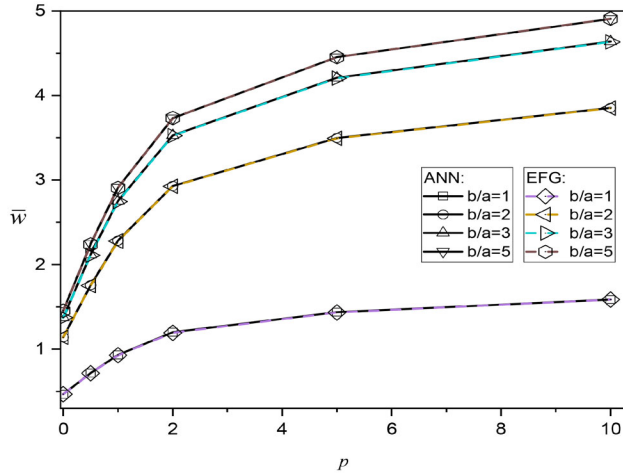
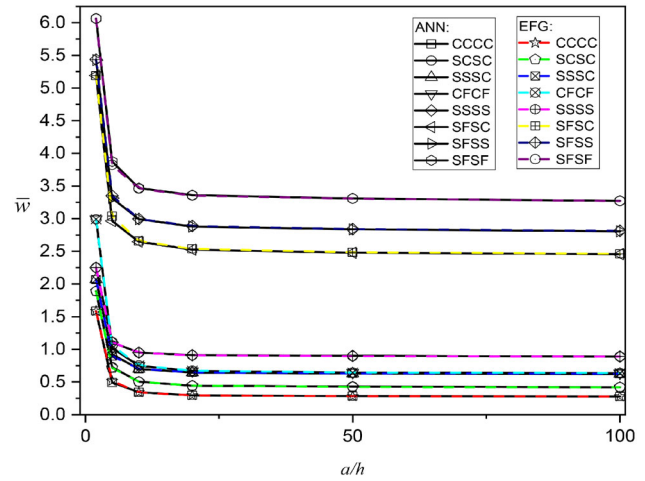
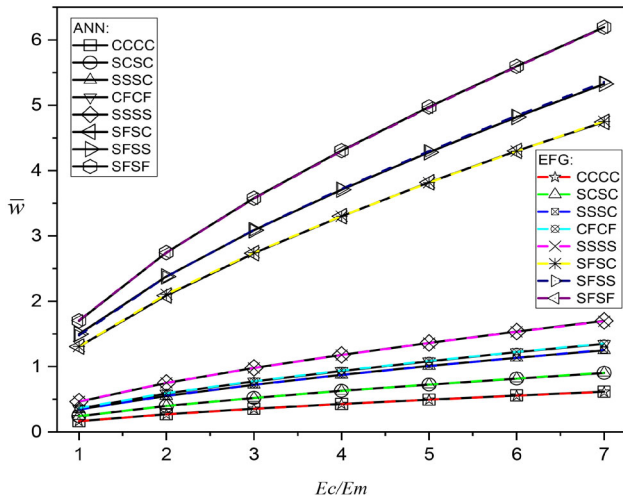
Model	Boundary conditions	Training performance	Training R-value	Testing performance	Testing R-value
1	CCCC	8.3661E-07	1.00000	1.0946E-04	0.99950
2	SCSC	1.8881E-05	0.99999	4.8793E-05	0.99996
3	SSSC	2.5183E-05	0.99999	2.6527E-04	0.99984
4	SSSS	1.1984E-05	0.99999	9.4593E-05	0.99993
5	SFSC	3.9477E-05	0.99999	8.1089E-04	0.99966
6	SFSS	2.6059E-05	0.99999	3.0789E-04	0.99985
7	CFCF	8.5723E-06	0.99999	1.0066E-04	0.99934
8	SFSF	1.5476E-05	1.00000	3.2398E-04	0.99984

carried out along with variations in aspect ratio (b/a) and volume fraction exponent (p) (Figure 10 and Table 7). The EFG method takes slightly more time compared to FEM. But the EFG results are more accurate than the FEM results. Hence, the accuracy offered by the EFG method makes up the time consumed in generating results. However, once the EFG-ANN model is developed, the time expense of result generation is reduced manifold. A detailed comparison

between the FEM, EFG, and ANN methods in terms of time and accuracy is given in Table 7. The current EFG-ANN model results in a 99.94% decrease in computational time as compared to the EFG method. The results are also compared for varying E_c/E_m ratio and a/h ratio (for Al/ZrO₂ square plate) under different boundary conditions (Figures 11 and 12). From the comparison studies, it is noticed that the predicted results of the ANN model and the

Table 7. Comparison of dimensionless transverse displacements \bar{w} of an $\text{Al}/\text{Al}_2\text{O}_3$ under UDL with SSSS boundary conditions ($a/h = 10$, $p = 5$).

Method	\bar{w}				Computational Time (sec)			
	FEM	EFG	EFG-ANN	Analytical [95]	FEM	EFG	EFG-ANN	Percentage Time Saved (%)
$b/a = 1$	1.4231	1.4351	1.4386	1.4360	77	99	0.061	99.94
$b/a = 2$	3.4468	3.4915	3.4952	3.4976	75	90	0.059	99.93
$b/a = 3$	4.4162	4.2030	4.2088	4.2066	79	93	0.062	99.93
$b/a = 4$	4.3391	4.4017	4.4021	4.4031	77	96	0.057	99.94
$b/a = 5$	4.3851	4.4537	4.4533	4.4537	76	93	0.060	99.94

**Figure 10.** Comparison and variation of dimensionless maximum transverse displacement \bar{w} versus aspect ratio (b/a) and volume fraction exponent (p) of an SSSS $\text{Al}/\text{Al}_2\text{O}_3$ rectangular FGM plate ($a/h = 10$).**Figure 12.** Comparison and variation of dimensionless maximum transverse displacement \bar{w} versus thickness ratio a/h for different boundary conditions of an Al/ZrO_2 square plate ($p = 5$).**Figure 11.** Comparison and variation of dimensionless maximum transverse displacement \bar{w} versus E_c/E_m ratio of a square FGM plate ($a/h = 10$, $p = 5$) for different boundary conditions under uniform loading.

results from analytical and EFG methods are in excellent agreement.

3.3. Results of the EFG-ANN model

3.3.1. Numerical discussion based on parametric studies

This section conducts parametric studies on the static behavior of FGM plates utilizing an artificial neural network model and EFG method. The study encompasses an examination of plates with different boundary conditions, ratios of side-to-thickness, and indices of volume fraction. A

comprehensive analysis of the transverse displacement of FGM plates subjected to uniform load for various thickness ratios (a/h), boundary conditions, and exponents of volume fraction (p) has been performed and the results are shown.

From a detailed study of the results from the EFG-ANN model and EFG method, the conclusions drawn are as follows:

1. The dimensionless maximum transverse displacement increases with an increase in the value of b/a and p regardless of the other parameters (Figure 10).
2. The dimensionless maximum transverse displacement increases as the ratio of E_c to E_m increases regardless of the other parameters and also increases with the release of the constraints of boundary conditions (Figure 11).
3. When the ratio of a to h increases, the dimensionless maximum transverse displacement decreases for all boundary conditions regardless of the other parameters (Figure 12).
4. The highest dimensionless maximum transverse displacement is obtained with the SFSF boundary condition, whereas the least is seen with the CCCC boundary condition.
5. The dimensionless maximum transverse displacement of the FGM plate with SFSF, SFSS, and SFSC boundary conditions is much higher than the transverse displacement values obtained under other boundary conditions.
6. Despite the fact that the two edges of the plate in the CFCF boundary condition are free, the maximum dimensionless transverse displacement obtained from

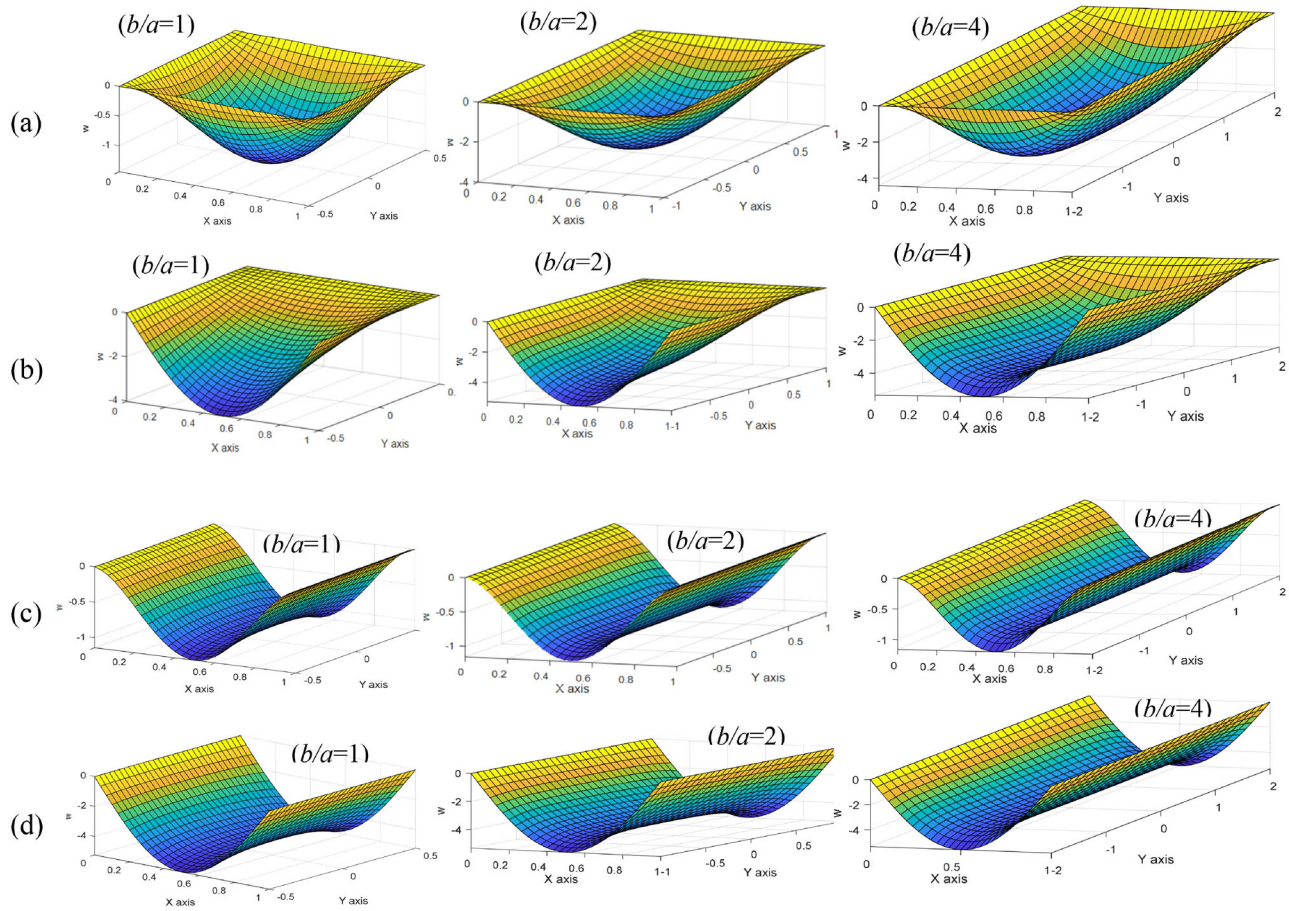


Figure 13. Transverse dimensionless displacement profile of an Al/Al₂O₃ plate for various Boundary Conditions and aspect ratios with $p = 5$ and $a/h = 10$ under uniform loading (a) SSSS and (b) SFSC. (c) CFCF and (d) SFSE.

the CFCF boundary condition of the FGM plate is lower than that obtained from the SSSS boundary conditions.

3.3.2. Discussion based on advantages of the EFG-ANN model

The developed EFG-ANN model predicts the deflection at each point of the plate with explicit accuracy at very less time expense as compared to other analytical and numerical methods. This quick result prediction of the model makes it easier to generate deflection profiles. Since the computational time is just a fraction of a second for each point, the plate can be discretized using an increased number of meshes, which will further increase the accuracy and make the deflection profiles smoother without spending too much time. Figure 13 shows the transverse dimensionless displacement profiles of an Al/Al₂O₃ plate for various boundary conditions and aspect ratios with $p = 5$ and $a/h = 10$ under uniform loading (a)SSSS (b)SFSC (c)CFCF (d)SFSE. The figure shows how the deflection profile varies according to the increase in aspect ratio for various boundary conditions. Each deflection profile given in the figure is generated within a second (currently it takes 0.5 s).

For a particular material or a problem, where all other parameters vary, we can generate the results as given in Table 8. In the table, the dimensionless maximum transverse displacement of an Al/Al₂O₃ square plate under uniform load for different boundary conditions, power law index, and thickness ratio are mentioned. It takes only 2.3 s to generate the data given in Table 8.

4. Conclusions

The analytical solution has the major drawback of being too difficult to implement in engineering practice when dealing with issues of dealing with different combinations of boundary conditions and complex geometry. In addition, a mathematical model to obtain accurate results with less computation time is the need of the hour. Therefore, the current study presents the theoretical formulation and the solutions using the EFG meshless method based on a higher-order displacement model with nine degrees of freedom (HSdT9) for the static deformation of Functionally Graded Material (FGM) plates. Further, an effective Artificial Neural Network (ANN) prediction model for predicting deflections of FGM plates is constructed and trained using the validated EFG results to obtain transverse displacements with less time. When the eight boundary conditions

Table 8. Dimensionless maximum transverse displacement \bar{w} of an $\text{Al}/\text{Al}_2\text{O}_3$ square plate under uniform load.

a/h	p	CCCC	SCSC	SSSC	SSSS	SFSC	SFSS	CFCF	SFSF
2	0	0.7006	0.8440	0.9235	1.0066	2.3982	2.5087	1.3276	2.8029
	0.5	0.9803	1.1958	1.3265	1.4508	3.4816	3.6762	1.8513	4.1170
	1	1.2350	1.5172	1.6866	1.8491	4.4585	4.7138	2.3428	5.2783
	2	1.6547	2.0259	2.2468	2.4706	5.9056	6.2307	3.1471	6.9751
	5	2.4247	2.8942	3.1873	3.4866	8.0188	8.3926	4.6128	9.3771
5	0	0.2345	0.3333	0.4180	0.5331	1.4575	1.6224	0.4772	1.8327
	0.5	0.3440	0.5007	0.6315	0.8106	2.2079	2.4606	0.7033	2.8031
	1	0.4411	0.6448	0.8221	1.0492	2.8529	3.1831	0.9025	3.6339
	2	0.5817	0.8436	1.0766	1.3614	3.6932	4.1219	1.1820	4.6986
	5	0.7764	1.1045	1.3647	1.6956	4.5636	5.0493	1.5637	5.7710
10	0	0.1657	0.2411	0.3358	0.4667	1.3056	1.4780	0.3645	1.7026
	0.5	0.2499	0.3701	0.5190	0.7182	2.0013	2.2717	0.5550	2.6297
	1	0.3230	0.4793	0.6796	0.9322	2.5979	2.9471	0.7201	3.4190
	2	0.4193	0.6192	0.8790	1.2000	3.3522	3.7839	0.9275	4.3839
	5	0.5222	0.7650	1.0639	1.4386	4.0302	4.5142	1.1419	5.2449
20	0	0.0821	0.1259	0.1807	0.2589	0.7436	0.8494	0.2120	0.9743
	0.5	0.1259	0.1912	0.2789	0.4054	1.2634	1.4263	0.3296	1.6689
	1	0.1657	0.2411	0.3358	0.4667	1.3056	1.4780	0.3645	1.7026
	2	0.2147	0.3252	0.4785	0.6872	1.9041	2.1726	0.4921	2.5273
	5	0.2788	0.4208	0.6258	0.8921	2.4667	2.8248	0.6397	3.2882
50	0	0.0466	0.0714	0.1058	0.1492	0.4246	0.4712	0.1067	0.5489
	0.5	0.0714	0.1058	0.1492	0.2076	0.5307	0.5927	0.1362	0.6202
	1	0.0921	0.1395	0.2012	0.2788	0.4208	0.6258	0.0892	1.0515
	2	0.1259	0.1912	0.2789	0.4054	1.2634	1.4263	0.3296	1.6689
	5	0.1657	0.2411	0.3358	0.4667	1.3056	1.4780	0.3645	1.7026
100	0	0.0234	0.0333	0.0418	0.0533	0.1457	0.1622	0.0477	0.1832
	0.5	0.0333	0.0500	0.0631	0.0810	0.2207	0.2460	0.0703	0.2803
	1	0.0411	0.0644	0.0822	0.1049	0.2852	0.3183	0.0902	0.3633
	2	0.0581	0.0843	0.1076	0.1361	0.3693	0.4121	0.1182	0.4698
	5	0.0776	0.1104	0.1364	0.1695	0.4563	0.5049	0.1563	0.5710

are given as inputs to develop a single ANN model, the accuracy of the model is badly affected. So, eight distinct models corresponding to eight different boundary conditions are developed and combined into a single ANN model for greater accuracy. More data points are used during the training of the model that considers eight parameters that could potentially affect the deflection. Based on the current study using the developed EFG-ANN model the following conclusions can be drawn.

- The deformation can be obtained with greater accuracy using the EFG approach with HSDT9, and the anticipated results show strong agreement with the analytical solutions provided by the same higher-order model.
- The validation and comparison of the generated results in the present investigation with the other analysis methods revealed that the EFG method and the EFG-ANN model give more accurate results than the FEM and other meshless methods (MLPG, KP-Ritz, Collocation).
- In place of the computationally intensive analytical procedures and expensive numerical analysis for the complex problems of FGM plates, the EFG-ANN model presented here is a potential alternative that consumes less computational time. In comparison to the EFG method, the current EFG-ANN model reduces computational time by 99.94 percent.

- The developed EFG-ANN model is capable of analyzing the eight various FGM plate boundary conditions.
- The developed EFG-ANN model can predict accurately the transverse displacements for uniformly and sinusoidally loaded plates with E_c/E_m ratio ranging from 1 to 7, aspect ratio ranging from 0.5 to 5, thickness ratio 2 to 100, and power law index value ranging from 0 to 10.
- The generation of deflection profiles takes a very short space of time and makes it conducive to increasing the mesh size to get smoother profiles.

The more precise results from the parametric studies will serve as a good reference for future research. The model might be expanded in the future to include vibration and buckling properties. Improvements can be made so that it applies to a wide variety of plate geometries (such as circular or quadrilateral).

Disclosure statement

The authors report there are no competing interests to declare.

References

- [1] J.K. Nath, and T. Das, Static and free vibration analysis of multilayered functionally graded shells and plates using an efficient zigzag theory, *Mech. Adv. Mater. Struct.*, vol. 26, no. 9, pp. 770–788, 2019. DOI: [10.1080/15376494.2017.1410915](https://doi.org/10.1080/15376494.2017.1410915).
- [2] K. Swaminathan, D.T. Naveenkumar, A.M. Zenkour, and E. Carrera, Stress, vibration and buckling analyses of FGM plates—A state-of-the-art review, *Compos. Struct.*, vol. 120, pp. 10–31, 2015. DOI: [10.1016/j.compstruct.2014.09.070](https://doi.org/10.1016/j.compstruct.2014.09.070).
- [3] H.T. Thai, and S.E. Kim, A review of theories for the modeling and analysis of functionally graded plates and shells, *Compos. Struct.*, vol. 128, pp. 70–86, 2015. DOI: [10.1016/j.compstruct.2015.03.010](https://doi.org/10.1016/j.compstruct.2015.03.010).
- [4] G. Kirchhoff, Über das Gleichgewicht und die Bewegung, *J. Reine Angew. Math.*, vol. 40, pp. 51–88, 1850.
- [5] J.N. Reddy, A simple higher-order theory for laminated composite plates, *J. Appl. Mech. Trans. ASME*, vol. 51, no. 4, pp. 745–752, 1984. DOI: [10.1115/1.3167719](https://doi.org/10.1115/1.3167719).
- [6] E. Carrera, Transverse normal stress effects in multilayered plates, *J. Appl. Mech. Trans. ASME*, vol. 66, no. 4, pp. 1004–1012, 1999. DOI: [10.1115/1.2791769](https://doi.org/10.1115/1.2791769).
- [7] E. Carrera, CZ requirements—models for the two dimensional analysis of multilayered structures, *Compos. Struct.*, vol. 37, no. 3–4, pp. 373–383, 1997. DOI: [10.1016/S0263-8223\(98\)80005-6](https://doi.org/10.1016/S0263-8223(98)80005-6).
- [8] E. Carrera, A priori vs. a posteriori evaluation of transverse stresses in multilayered orthotropic plates, *Compos. Struct.*, vol. 48, no. 4, pp. 245–260, 2000. DOI: [10.1016/S0263-8223\(99\)00112-9](https://doi.org/10.1016/S0263-8223(99)00112-9).
- [9] J.L. Mantari, I.A. Ramos, E. Carrera, and M. Petrolo, Static analysis of functionally graded plates using new non-polynomial displacement fields via Carrera Unified Formulation, *Compos. B Eng.*, vol. 89, pp. 127–142, 2016. DOI: [10.1016/j.compositesb.2015.11.025](https://doi.org/10.1016/j.compositesb.2015.11.025).
- [10] Z. Nouri, S. Sarrami-Foroushani, F. Azhari, and M. Azhari, Application of Carrera unified formulation in conjunction with finite strip method in static and stability analysis of functionally graded plates, *Mech. Adv. Mater. Struct.*, vol. 29, no. 2, pp. 250–266, 2022. DOI: [10.1080/15376494.2020.1762265](https://doi.org/10.1080/15376494.2020.1762265).
- [11] E. Carrera, A study of transverse normal stress effect on vibration of multilayered plates and shells, *J. Sound Vib.*, vol. 225, no. 5, pp. 803–829, 1999. DOI: [10.1006/jsvi.1999.2271](https://doi.org/10.1006/jsvi.1999.2271).

- [12] E. Carrera, Layer-wise mixed models for accurate vibrations analysis of multilayered plate, *J. Appl. Mech. Trans. ASME*, vol. 65, no. 4, pp. 820–828, 1998. DOI: [10.1115/1.2791917](#).
- [13] E. Carrera, Mixed layer-wise models for multilayered plates analysis, *Compos. Struct.*, vol. 43, no. 1, pp. 57–70, 1998. DOI: [10.1016/S0263-8223\(98\)00097-X](#).
- [14] E. Carrera, Multilayered shell theories accounting for layerwise mixed description, Part 1: governing equations, *Aiaa J.*, vol. 37, no. 9, pp. 1107–1116, 1999. DOI: [10.2514/2.821](#).
- [15] E. Carrera, Evaluation of layerwise mixed theories for laminated plates analysis, *Aiaa J.*, vol. 36, no. 5, pp. 830–839, 1998. DOI: [10.2514/2.444](#).
- [16] E. Carrea, A Reissner's mixed variational theorem applied to vibration analysis of multilayered shell, *J. Appl. Mech.*, vol. 66, pp. 69–78, 1999.
- [17] E. Carrera, Single-vs multilayer plate modelings on the basis of Reissner's mixed theorem, *Aiaa J.*, vol. 38, no. 2, pp. 342–352, 2000. DOI: [10.2514/2.962](#).
- [18] S. Chakraverty, and K.K. Pradhan, Free vibration of exponential functionally graded rectangular plates in thermal environment with general boundary conditions, *Aerosp. Sci. Technol.*, vol. 36, pp. 132–156, 2014. DOI: [10.1016/j.ast.2014.04.005](#).
- [19] M. Ruan, and Z.M. Wang, Transverse vibrations of moving skew plates made of functionally graded material, *J. Vib. Control.*, vol. 22, no. 16, pp. 3504–3517, 2016. DOI: [10.1177/1077546314563967](#).
- [20] E. Reissner, The effect of transverse shear deformation on the bending of laminated plates, *J. Appl. Mech.*, vol. 12, no. 2, pp. A69–A77, 1945. DOI: [10.1177/002199836900300316](#).
- [21] R.D. Mindlin, Influence of rotatory inertia and shear on flexural motions of isotropic, elastic plates, *J. Appl. Mech.*, vol. 18, no. 1, pp. 31–38, 1951. DOI: [10.1115/1.4010217](#).
- [22] B.N. Pandya, and T. Kant, Finite element analysis of laminated composite plates using a higher-order displacement model, *Compos. Sci. Technol.*, vol. 32, no. 2, pp. 137–155, 1988. DOI: [10.1016/0266-3538\(88\)90003-6](#).
- [23] T. Kant, and B.S. Manjunatha, An unsymmetric FRC laminate C° finite element model with 12 degrees of freedom per node, *Eng. Comput.*, vol. 5, no. 4, pp. 300–308, 1988. DOI: [10.1108/eb023749](#).
- [24] B.N. Pandya, and T. Kant, Higher-order shear deformable theories for flexure of sandwich plates-Finite element evaluations, *Int. J. Solids Struct.*, vol. 24, no. 12, pp. 1267–1286, 1988. DOI: [10.1016/0020-7683\(88\)90090-X](#).
- [25] A.M. Zenkour, and Z.S. Hafed, Bending analysis of functionally graded piezoelectric plates via quasi-3D trigonometric theory, *Mech. Adv. Mater. Struct.*, vol. 27, no. 18, pp. 1551–1562, 2020. DOI: [10.1080/15376494.2018.1516325](#).
- [26] M. Zidi, A. Tounsi, M.S.A. Houari, E.A. Adda Bedia, and O. Anwar Bég, Bending analysis of FGM plates under hygro-thermo-mechanical loading using a four variable refined plate theory, *Aerosp. Sci. Technol.*, vol. 34, no. 1, pp. 24–34, 2014. DOI: [10.1016/j.ast.2014.02.001](#).
- [27] H. Frahli, R. Bennai, M. Nebab, H. Ait Atmane, and A. Tounsi, Assessing effects of parameters of viscoelastic foundation on the dynamic response of functionally graded plates using a novel HSDT theory, *Mech. Adv. Mater. Struct.*, vol. 30, no. 13, pp. 2765–2779, 2023. DOI: [10.1080/15376494.2022.2062632](#).
- [28] R. Ma, and Q. Jin, Buckling analysis of sandwich plates with functionally graded graphene reinforced composite face sheets based on a five-unknown plate theory, *Mech. Adv. Mater. Struct.*, vol. 29, no. 28, pp. 7431–7440, 2022. DOI: [10.1080/15376494.2021.2000078](#).
- [29] S. Xiong, C. Zhou, X. Zheng, D. An, D. Xu, Z. Hu, Y. Zhao, R. Li, and B. Wang, New analytic thermal buckling solutions of non-Lévy-type functionally graded rectangular plates by the symplectic superposition method, *Acta Mech.*, vol. 233, no. 7, pp. 2955–2968, 2022. DOI: [10.1007/s00707-022-03258-8](#).
- [30] S. Xiong, C. Zhou, L. Zhao, X. Zheng, Y. Zhao, B. Wang, and R. Li, Symplectic framework-based new analytic solutions for thermal buckling of temperature-dependent moderately thick functionally graded rectangular Plates, *Int. J. Str. Stab. Dyn.*, vol. 22, no. 14, pp. 1–23, 2022. DOI: [10.1142/S0219455422501541](#).
- [31] Z. Hu, C. Zhou, X. Zheng, Z. Ni, and R. Li, Free vibration of non-Lévy-type functionally graded doubly curved shallow shells: new analytic solutions, *Compos. Struct.*, vol. 304, no. P2, pp. 116389, 2023. DOI: [10.1016/j.compstruct.2022.116389](#).
- [32] Z. Hu, Y. Shi, S. Xiong, X. Zheng, and R. Li, New analytic free vibration solutions of non-Lévy-type porous FGM rectangular plates within the symplectic framework, *Thin-Walled Struct.*, vol. 185, pp. 110609, 2023. DOI: [10.1016/j.tws.2023.110609](#).
- [33] J.A.T. Barbosa, and A.J.M. Ferreira, Geometrically nonlinear analysis of functionally graded plates and shells, *Mech. Adv. Mater. Struct.*, vol. 17, no. 1, pp. 40–48, 2009. DOI: [10.1080/15376490903082870](#).
- [34] K. Koutoati, F. Mohri, and E.M. Daya, Finite element approach of axial bending coupling on static and vibration behaviors of functionally graded material sandwich beams, *Mech. Adv. Mater. Struct.*, vol. 28, no. 15, pp. 1537–1553, 2021. DOI: [10.1080/15376494.2019.1685144](#).
- [35] P. Vidal, L. Gallimard, O. Polit, and E. Valot, Analysis of functionally graded plates based on a variable separation method, *Mech. Adv. Mater. Struct.*, vol. 29, no. 26, pp. 4890–4901, 2022. DOI: [10.1080/15376494.2021.1942597](#).
- [36] S. Hirannaiah, K. Swaminathan, and T. Rajanna, Thermo-mechanical vibration and buckling analysis of porous FG sandwich plates with geometric discontinuity based on physical neutral surface, *Mech. Adv. Mater. Struct.*, pp. 1–25, 2023. DOI: [10.1080/15376494.2023.2220493](#).
- [37] G.R. Liu, *Meshfree Methods: Moving beyond the Finite Element Method*, CRC Press, Boca Raton, FL, 2009.
- [38] J.-F. Remacle, J. Lambrechts, B. Seny, E. Marchandise, A. Johnen, and C. Geuzainet, Blossom-Quad: a non-uniform quadrilateral mesh generator using a minimum-cost perfect-matching algorithm, *Int. J. Numer. Meth. Engng.*, vol. 89, no. 9, pp. 1102–1119, 2012. DOI: [10.1002/nme](#).
- [39] G.R. Liu, and Y.T. Gu, *An Introduction to Meshfree Methods and Their Programming*, Springer Science & Business Media, Cham, 2005. DOI: [10.1017/CBO9781107415324.004](#).
- [40] Y. Chen, J.D. Lee, and A. Eskandarian, *Meshless Methods in Solid Mechanics (Vol. 9)*. Springer, New York, 2006. DOI: [10.1017/CBO9781107415324.004](#).
- [41] J.J. Monaghan, An introduction to SPH, *Comput. Phys. Commun.*, vol. 48, no. 1, pp. 89–96, 1988. DOI: [10.1016/0010-4655\(88\)90026-4](#).
- [42] P. Lancaster, and K. Salkauskas, Surfaces generated by moving least squares methods, *Math. Comp.*, vol. 37, no. 155, pp. 141–158, 1981. DOI: [10.2307/2007507](#).
- [43] E.J. Kansa, Multiquadrics-A scattered data approximation scheme with applications to computational fluid-dynamics-II solutions to parabolic, hyperbolic and elliptic partial differential equations, *Comput. Math. Appl.*, vol. 19, no. 8–9, pp. 147–161, 1990. DOI: [10.1016/0898-1221\(90\)90271-K](#).
- [44] E.J. Kansa, Multiquadrics-A scattered data approximation scheme with applications to computational fluid-dynamics-I surface approximations and partial derivative estimates, *Comput. Math. with Appl.*, vol. 19, no. 8–9, pp. 127–145, 1990. DOI: [10.1016/0898-1221\(90\)90270-T](#).
- [45] A.J.M. Ferreira, A formulation of the multiquadric radial basis function method for the analysis of laminated composite plates, *Compos. Struct.*, vol. 59, no. 3, pp. 385–392, 2003. DOI: [10.1016/S0263-8223\(02\)00239-8](#).
- [46] T. Belytschko, Y.Y. Lu, and L. Gu, Element-free galerkin methods, *Int. J. Numer. Methods Eng.*, vol. 37, no. 2, pp. 229–256, 1994.
- [47] T. Belytschko, L. Gu, and Y.Y. Lu, Fracture and crack growth by element free Galerkin methods, *Modelling Simul. Mater. Sci.*

- Eng., vol. 2, no. 3A, pp. 519–534, 1994. DOI: [10.1088/0965-0393/2/3A/007](https://doi.org/10.1088/0965-0393/2/3A/007).
- [48] A.Y. Tamijani, and R.K. Kapania, Vibration analysis of curvilinearly-stiffened functionally graded plate using element free galerkin method, *Mech. Adv. Mater. Struct.*, vol. 19, no. 1–3, pp. 100–108, 2012. DOI: [10.1080/15376494.2011.572240](https://doi.org/10.1080/15376494.2011.572240).
- [49] Wing Kam Liu, Sukky Jun, and Yi Fei Zhang, Reproducing kernel particle methods, *Int. J. Numer. Meth. Fluids*, vol. 20, no. 8–9, pp. 1081–1106, 1995. DOI: [10.1002/flid.1650200824](https://doi.org/10.1002/flid.1650200824).
- [50] Y.Y. Lee, X. Zhao, and K.M. Liew, Thermoelastic analysis of functionally graded plates using the element-free kp-Ritz method, *Smart Mater. Struct.*, vol. 18, no. 3, pp. 035007, 2009. DOI: [10.1088/0964-1726/18/3/035007](https://doi.org/10.1088/0964-1726/18/3/035007).
- [51] X. Zhao, and K.M. Liew, Geometrically nonlinear analysis of functionally graded plates using the element-free kp-Ritz method, *Comput. Methods Appl. Mech. Eng.*, vol. 198, no. 33–36, pp. 2796–2811, 2009. DOI: [10.1016/j.cma.2009.04.005](https://doi.org/10.1016/j.cma.2009.04.005).
- [52] G.E. Fasshauer, Solving partial differential equations by collocation with radial basis functions, *Proceedings of Chamonix*, 1997. pp. 1–8.
- [53] F. Fabbrocino, S. Saitta, R. Vescovini, N. Fantuzzi, and R. Luciano, Meshless computational strategy for higher order strain gradient plate models, *MCA.*, vol. 27, no. 2, pp. 19, 2022. DOI: [10.3390/mca27020019](https://doi.org/10.3390/mca27020019).
- [54] C.M.C. Roque, A.J.M. Ferreira, A.M.A. Neves, G.E. Fasshauer, C.M.M. Soares, and R.M.N. Jorge, Dynamic analysis of functionally graded plates and shells by radial basis functions, *Mech. Adv. Mater. Struct.*, vol. 17, no. 8, pp. 636–652, 2010. DOI: [10.1080/15376494.2010.518932](https://doi.org/10.1080/15376494.2010.518932).
- [55] A.M.A. Neves, A.J.M. Ferreira, E. Carrera, C.M.C. Roque, M. Cinefra, R.M.N. Jorge, and C.M.M. Soares, Bending of FGM plates by a sinusoidal plate formulation and collocation with radial basis functions, *Mech. Res. Commun.*, vol. 38, no. 5, pp. 368–371, 2011. DOI: [10.1016/j.mechrescom.2011.04.011](https://doi.org/10.1016/j.mechrescom.2011.04.011).
- [56] A.J.M. Ferreira, C.M.C. Roque, R.M.N. Jorge, G.E. Fasshauer, and R.C. Batra, Analysis of functionally graded plates by a robust meshless method, *Mech. Adv. Mater. Struct.*, vol. 14, no. 8, pp. 577–587, 2007. DOI: [10.1080/15376490701672732](https://doi.org/10.1080/15376490701672732).
- [57] S.N. Atluri, and T. Zhu, A new meshless local Petrov-Galerkin (MLPG) approach in computational mechanics, *Comput. Mech.*, vol. 22, no. 2, pp. 117–127, 1998. DOI: [10.1007/s004660050346](https://doi.org/10.1007/s004660050346).
- [58] J. Sladek, V. Sladek, C. Zhang, and P. Sulek, Static and dynamic analysis of shallow shells with functionally graded and orthotropic material properties, *Mech. Adv. Mater. Struct.*, vol. 15, no. 2, pp. 142–156, 2008. DOI: [10.1080/15376490701810480](https://doi.org/10.1080/15376490701810480).
- [59] J.G. Wang, and G.R. Liu, A point interpolation meshless method based on radial basis functions, *Int. J. Numer. Meth. Engng.*, vol. 54, no. 11, pp. 1623–1648, 2002. DOI: [10.1002/nme.489](https://doi.org/10.1002/nme.489).
- [60] S. Saitta, R. Luciano, R. Vescovini, N. Fantuzzi, and F. Fabbrocino, Free vibrations and buckling analysis of cross-ply composite nanoplates by means of a mesh free radial point interpolation method, *Compos. Struct.*, vol. 298, pp. 115989, 2022. DOI: [10.1016/j.compstruct.2022.115989](https://doi.org/10.1016/j.compstruct.2022.115989).
- [61] L. Gu, Moving kriging interpolation and element-free Galerkin method, *Int. J. Numer. Meth. Engng.*, vol. 56, no. 1, pp. 1–11, 2003. DOI: [10.1002/nme.553](https://doi.org/10.1002/nme.553).
- [62] X.G. Li, B.D. Dai, and L.H. Wang, A moving Kriging interpolation-based boundary node method for two-dimensional potential problems, *Chinese Phys. B.*, vol. 19, no. 12, pp. 120202, 2010. DOI: [10.1088/1674-1056/19/12/120202](https://doi.org/10.1088/1674-1056/19/12/120202).
- [63] L.F. Qian, R.C. Batra, and L.M. Chen, Static and dynamic deformations of thick functionally graded elastic plates by using higher-order shear and normal deformable plate theory and meshless local Petrov-Galerkin method, *Compos. B Eng.*, vol. 35, no. 6–8, pp. 685–697, 2004. DOI: [10.1016/j.compositesb.2004.02.004](https://doi.org/10.1016/j.compositesb.2004.02.004).
- [64] D.F. Gilhooley, R.C. Batra, J.R. Xiao, M.A. McCarthy, and J.W. Gillespie, Analysis of thick functionally graded plates by using higher-order shear and normal deformable plate theory and MLPG method with radial basis functions, *Compos. Struct.*, vol. 80, no. 4, pp. 539–552, 2007. DOI: [10.1016/j.compstruct.2006.07.007](https://doi.org/10.1016/j.compstruct.2006.07.007).
- [65] P. Zhu, L.W. Zhang, and K.M. Liew, Geometrically nonlinear thermomechanical analysis of moderately thick functionally graded plates using a local Petrov-Galerkin approach with moving Kriging interpolation, *Compos. Struct.*, vol. 107, no. 1, pp. 298–314, 2014. DOI: [10.1016/j.compstruct.2013.08.001](https://doi.org/10.1016/j.compstruct.2013.08.001).
- [66] R. Vaghefi, M.R. Hematiyan, and A. Nayebi, Three-dimensional thermo-elastoplastic analysis of thick functionally graded plates using the meshless local Petrov-Galerkin method, *Eng. Anal. Bound. Elem.*, vol. 71, pp. 34–49, 2016. DOI: [10.1016/j.enganabound.2016.07.001](https://doi.org/10.1016/j.enganabound.2016.07.001).
- [67] M. Rashidi Moghaddam, and G.H. Baradaran, Three-dimensional free vibrations analysis of functionally graded rectangular plates by the meshless local Petrov-Galerkin (MLPG) method, *Appl. Math. Comput.*, vol. 304, pp. 153–163, 2017. DOI: [10.1016/j.amc.2017.01.049](https://doi.org/10.1016/j.amc.2017.01.049).
- [68] V.S. Khorasani, and M. Bayat, Bending analysis of FG plates using a general third-order plate theory with modified couple stress effect and MLPG method, *Eng. Anal. Bound. Elem.*, vol. 94, pp. 159–171, 2018. DOI: [10.1016/j.enganabound.2018.06.015](https://doi.org/10.1016/j.enganabound.2018.06.015).
- [69] D.H. Konda, J.A.F. Santiago, J.C.F. Telles, J.P.F. Mello, and E.G.A. Costa, A meshless Reissner plate bending procedure using local radial point interpolation with an efficient integration scheme, *Eng. Anal. Bound. Elem.*, vol. 99, pp. 46–59, 2019. DOI: [10.1016/j.enganabound.2018.11.004](https://doi.org/10.1016/j.enganabound.2018.11.004).
- [70] A.J.M. Ferreira, R.C. Batra, C.M.C. Roque, L.F. Qian, and R.M.N. Jorge, Natural frequencies of functionally graded plates by a meshless method, *Compos. Struct.*, vol. 75, no. 1–4, pp. 593–600, 2006. DOI: [10.1016/j.compstruct.2006.04.018](https://doi.org/10.1016/j.compstruct.2006.04.018).
- [71] A.M.A. Neves, A.J.M. Ferreira, E. Carrera, C.M.C. Roque, M. Cinefra, R.M.N. Jorge, and C.M.M. Soares, A quasi-3D sinusoidal shear deformation theory for the static and free vibration analysis of functionally graded plates, *Compos. B Eng.*, vol. 43, no. 2, pp. 711–725, 2012. DOI: [10.1016/j.compositesb.2011.08.009](https://doi.org/10.1016/j.compositesb.2011.08.009).
- [72] S. Xiang, and G.W. Kang, A nth-order shear deformation theory for the bending analysis on the functionally graded plates, *Eur. J. Mech. A/Solids.*, vol. 37, pp. 336–343, 2013. DOI: [10.1016/j.euromechsol.2012.08.005](https://doi.org/10.1016/j.euromechsol.2012.08.005).
- [73] R. Kumar, A. Lal, B.N. Singh, and J. Singh, New transverse shear deformation theory for bending analysis of FGM plate under patch load, *Compos. Struct.*, vol. 208, pp. 91–100, 2019. DOI: [10.1016/j.compstruct.2018.10.014](https://doi.org/10.1016/j.compstruct.2018.10.014).
- [74] S. Hosseini, G. Rahimi, and Y. Anani, A meshless collocation method based on radial basis functions for free and forced vibration analysis of functionally graded plates using FSDT, *Eng. Anal. Bound. Elem.*, vol. 125, pp. 168–177, 2021. DOI: [10.1016/j.enganabound.2020.12.016](https://doi.org/10.1016/j.enganabound.2020.12.016).
- [75] X. Zhao, Y.Y. Lee, and K.M. Liew, Free vibration analysis of functionally graded plates using the element-free kp-Ritz method, *J. Sound Vib.*, vol. 319, no. 3–5, pp. 918–939, 2009. DOI: [10.1016/j.jsv.2008.06.025](https://doi.org/10.1016/j.jsv.2008.06.025).
- [76] S. Kaewumpai, and A. Luadsong, Two-field-variable meshless method based on moving kriging interpolation for solving simply supported thin plates under various loads, *J. King Saud Univ. Sci.*, vol. 27, no. 3, pp. 209–216, 2015. DOI: [10.1016/j.jksus.2014.12.003](https://doi.org/10.1016/j.jksus.2014.12.003).
- [77] T. Van Vu, N.H. Nguyen, A. Khosravifard, M.R. Hematiyan, S. Tanaka, and T.Q. Bui, A simple FSDT-based meshfree method for analysis of functionally graded plates, *Eng. Anal. Bound. Elem.*, vol. 79, pp. 1–12, 2017. DOI: [10.1016/j.enganabound.2017.03.002](https://doi.org/10.1016/j.enganabound.2017.03.002).
- [78] T. Van Vu, A. Khosravifard, M.R. Hematiyan, and T.Q. Bui, A new refined simple TSDT-based effective meshfree method for analysis of through-thickness FG plates, *Appl. Math. Model.*, vol. 57, pp. 514–534, 2018. DOI: [10.1016/j.apm.2018.01.004](https://doi.org/10.1016/j.apm.2018.01.004).

- [79] T. Van Vu, A. Khosravifard, M.R. Hematiyan, and T.Q. Bui, Enhanced meshfree method with new correlation functions for functionally graded plates using a refined inverse sin shear deformation plate theory, *Eur. J. Mech. A/Solids*, vol. 74, pp. 160–175, 2019. DOI: [10.1016/j.euromechsol.2018.11.005](https://doi.org/10.1016/j.euromechsol.2018.11.005).
- [80] M. Memar Ardestani, B. Soltani, and S. Shams, Analysis of functionally graded stiffened plates based on FSDT utilizing reproducing kernel particle method, *Compos. Struct.*, vol. 112, no. 1, pp. 231–240, 2014. DOI: [10.1016/j.compstruct.2014.01.032](https://doi.org/10.1016/j.compstruct.2014.01.032).
- [81] T.T. Truong, V.S. Lo, M.N. Nguyen, N.T. Nguyen, and K.D. Nguyen, A novel meshfree radial point interpolation method with discrete shear gap for nonlinear static analysis of functionally graded plates, *Eng. Comput.*, no. 0123456789, pp. 1–21, 2022. DOI: [10.1007/s00366-022-01691-w](https://doi.org/10.1007/s00366-022-01691-w).
- [82] V.N. Van Do, and C.H. Lee, Nonlinear analyses of FGM plates in bending by using a modified radial point interpolation mesh-free method, *Appl. Math. Model.*, vol. 57, pp. 1–20, 2018. DOI: [10.1016/j.apm.2017.12.035](https://doi.org/10.1016/j.apm.2017.12.035).
- [83] A. Jodaei, M. Jalal, and M.H. Yas, Free vibration analysis of functionally graded annular plates by state-space based differential quadrature method and comparative modeling by ANN, *Compos. B Eng.*, vol. 43, no. 2, pp. 340–353, 2012. DOI: [10.1016/j.compositesb.2011.08.052](https://doi.org/10.1016/j.compositesb.2011.08.052).
- [84] Yousef S. Al Rjoub, and J.A. Alshatnawi, Free vibration of functionally-graded porous cracked plates, *Structures*, vol. 28, pp. 2392–2403, 2020. DOI: [10.1016/j.istruc.2020.10.059](https://doi.org/10.1016/j.istruc.2020.10.059).
- [85] V. Kallannavar, S. Kattimani, M.E.M. Soudagar, M.A. Mujtaba, S. Alshahrani, and M. Imran, Neural network-based prediction model to investigate the influence of temperature and moisture on vibration characteristics of skew laminated composite sandwich plates, *Materials*, vol. 14, no. 12, pp. 3170, 2021. DOI: [10.3390/ma14123170](https://doi.org/10.3390/ma14123170).
- [86] T. T. Tran, P.C. Nguyen, and Q.H. Pham, Vibration analysis of FGM plates in thermal environment resting on elastic foundation using ES-MITC3 element and prediction of ANN, *Case Stud. Therm. Eng.*, vol. 24, no. December 2020, pp. 100852, 2021. DOI: [10.1016/j.csite.2021.100852](https://doi.org/10.1016/j.csite.2021.100852).
- [87] V. Mahesh, V. Mahesh, and S.A. Ponnusami, FEM-ANN approach to predict nonlinear pyro-coupled deflection of sandwich plates with agglomerated porous nanocomposite core and piezo-magneto-elastic facings in thermal environment, *Mech. Adv. Mater. Struct.*, pp. 1–24, 2023. DOI: [10.1080/15376494.2023.2201927](https://doi.org/10.1080/15376494.2023.2201927).
- [88] H.T. Duong, H.C. Phan, T.M. Tran, and A.S. Dhar, Assessment of critical buckling load of functionally graded plates using artificial neural network modeling, *Neural Comput. Applic.*, vol. 33, no. 23, pp. 16425–16437, 2021. DOI: [10.1007/s00521-021-06238-6](https://doi.org/10.1007/s00521-021-06238-6).
- [89] Q.H. Pham, P.C. Nguyen, and T.T. Tran, Free vibration response of auxetic honeycomb sandwich plates using an improved higher-order ES-MITC3 element and artificial neural network, *Thin-Walled Struct.*, vol. 175, no. December 2021, pp. 109203, 2022. DOI: [10.1016/j.tws.2022.109203](https://doi.org/10.1016/j.tws.2022.109203).
- [90] A. Carvalho, T. Silva, M.A.R. Loja, and F.R. Damásio, Assessing the influence of material and geometrical uncertainty on the mechanical behavior of functionally graded material plates, *Mech. Adv. Mater. Struct.*, vol. 24, no. 5, pp. 417–426, 2017. DOI: [10.1080/15376494.2016.1191100](https://doi.org/10.1080/15376494.2016.1191100).
- [91] M. Shakeri, and R. Mirzaeifar, Static and dynamic analysis of thick functionally graded plates with piezoelectric layers using layerwise finite element model, *Mech. Adv. Mater. Struct.*, vol. 16, no. 8, pp. 561–575, 2009. DOI: [10.1080/15376490802625514](https://doi.org/10.1080/15376490802625514).
- [92] S.R. Li, F. Zhang, and R.G. Liu, Classical and homogenized expressions for the bending solutions of FGM plates based on the four variable plate theories, *Mech. Adv. Mater. Struct.*, pp. 1–12, 2023. DOI: [10.1080/15376494.2023.2177909](https://doi.org/10.1080/15376494.2023.2177909).
- [93] S. Çeriba, Static and dynamic analyses of thin uniformly loaded super elliptical FGM plates, *Mech. Adv. Mater. Struct.*, vol. 19, no. 5, pp. 323–335, 2012. DOI: [10.1080/15376494.2010.528160](https://doi.org/10.1080/15376494.2010.528160).
- [94] K. Swaminathan, S. Hirannaiah, and T. Rajanna, Influence of porosity and nonuniform in-plane edge loads on vibration and buckling response of power law and sigmoid function based FG sandwich plates with geometrical discontinuities, *Mech. Based Des. Struct. Mach.*, pp. 1–33, 2022. DOI: [10.1080/15397734.2022.2107010](https://doi.org/10.1080/15397734.2022.2107010).
- [95] T.M. Tu, T.H. Quoc, and N.V. Long, Bending analysis of functionally graded plates using new eight-unknown higher order shear deformation theory, *Struct. Eng. Mech.*, vol. 62, no. 3, pp. 311–324, 2017. DOI: [10.12989/sem.2017.62.3.311](https://doi.org/10.12989/sem.2017.62.3.311).
- [96] A.M. Zenkour, Generalized shear deformation theory for bending analysis of functionally graded plates, *Appl. Math. Model.*, vol. 30, no. 1, pp. 67–84, 2006. DOI: [10.1016/j.apm.2005.03.009](https://doi.org/10.1016/j.apm.2005.03.009).
- [97] E. Carrera, S. Brischetto, M. Cinefra, and M. Soave, Effects of thickness stretching in functionally graded plates and shells, *Compos. B Eng.*, vol. 42, no. 2, pp. 123–133, 2011. DOI: [10.1016/j.compositesb.2010.10.005](https://doi.org/10.1016/j.compositesb.2010.10.005).
- [98] H.T. Thai, and D.H. Choi, Finite element formulation of various four unknown shear deformation theories for functionally graded plates, *Finite Elem. Anal. Des.*, vol. 75, pp. 50–61, 2013. DOI: [10.1016/j.finel.2013.07.003](https://doi.org/10.1016/j.finel.2013.07.003).